J. Fluid Mech. (2012), *vol.* 700, *pp.* 246–282.
doi:10.1017/jfm.2012.129

Pulsating pipe flow with large-amplitude oscillations in the very high frequency regime. Part 1. Time-averaged analysis

M. Manna[1], A. Vacca[2] and R. Verzicco[3,4]†

[1] Dipartimento di Ingegneria Meccanica per l'Energetica, Università di Napoli 'Federico II', via Claudio 21, 80125 Naples, Italy

[2] Dipartimento di Ingegneria Civile, Seconda Università di Napoli, via Roma 29, 81031 Aversa (CE), Italy

[3] Dipartimento di Ingegneria Meccanica, Università di Roma 'Tor Vergata', via del Politecnico 1, 00133 Rome, Italy

[4] Physics of Fluids Group, University of Twente, Drienerlolaan 5, 7522 NB Enschede, The Netherlands

(Received 8 June 2011; revised 15 February 2012; accepted 5 March 2012; first published online 25 April 2012)

This paper numerically investigates the effects of a harmonic volume forcing of prescribed frequency on the turbulent pipe flow at a Reynolds number, based on bulk velocity and pipe diameter, of 5900. The thickness of the Stokes layer, resulting from the oscillatory flow component, is a small fraction of the pipe radius and therefore the associated vorticity is confined within a few wall units. The harmonic forcing term is prescribed so that the ratio of the oscillating to the mean bulk velocity (β) ranges between 1 and 10.6. In all cases the oscillatory flow obeys the Stokes analytical velocity distribution while remarkable changes in the current component are observed. At intermediate values $\beta = 5$, a relaminarization process occurs, while for $\beta = 10.6$, turbulence is affected so much by the harmonic forcing that the near-wall coherent structures, although not fully suppressed, are substantially weakened. The present study focuses on the analysis of the time- and space-averaged statistics of the first- and second-order moments, vorticity fluctuations and Reynolds stress budgets. Since the flow is unsteady not only locally but also in its space-averaged dynamics, it can be analysed using phase-averaged and time-averaged statistics. While the former gives information about the statistics of the fluctuations about the mean, the latter, postponed to a subsequent paper, shows how the mean is affected by the fluctuations. Clearly, the two phenomena are connected and both of them deserve investigation.

Key words: pipe flow boundary layer, wave–turbulence interactions

1. Introduction

Many engineering problems are characterized by flow unsteadiness determined by a harmonic-like time-varying forcing superposed onto a stationary component; these flows are usually referred to as *pulsating* or *pulsatile* flows. Examples of relevant applications concern biological flows (pulmonary ventilation or blood flow in aortic

† Email address for correspondence: verzicco@uniroma2.it

and coronary arteries) and environmental flows (flow over the ocean bed or sediment transport in coastal water).

The oscillatory component of motion may be generated artificially by a rotating or popped valve, like those present in variable-displacement pumps, or it may result from an interaction problem. The steady or *current* flow is usually associated with a stationary pressure forcing. In fact, despite their great environmental and biomedical relevance, little is known about the physics of pulsating turbulent flows, even in simple geometries. One reason for this is the enhanced complexities yielded by the oscillatory component of motion, which increases the relevant similarity parameters from one (in the case of steady flow) to three (Akhavan, Kamm & Shapiro 1991).

Several theoretical studies on plane Poiseuille flow (Grosch & Salwen 1968; Herbert 1972; Hall 1975; von Kerczek 1982) have shown that a periodic flow modulation may stabilize the mean flow, depending on the amplitude and the frequency of the modulation itself. Hall (1975) and von Kerczek (1982) agree on the destabilizing effect on the plane Poiseuille flow at very high frequencies, while at intermediate frequencies the conclusions are not so neat (Grosch & Salwen 1968; von Kerczek 1982). Singer, Ferziger & Reed (1989) describe results from a direct numerical simulation (DNS) of the flow in a plane channel with imposed periodic unsteadiness, and indicate that the sinusoidal pulsations provide a stabilizing effect at all but very low frequencies.

The available literature on the stability of pulsating pipe flows is more limited. Tozzi & von Kerczek (1986) have shown that low-frequency oscillatory Hagen–Poiseuille flow is slightly more stable to axisymmetric disturbances than the steady flow. More importantly, the highly inflectional instantaneous velocity profiles do not lead to instantaneous instability, even for very low-frequency oscillation. Fedele, Hitt & Prabhub (2005), using a set of eigenfunctions derived from the long-wave limit of the Orr–Sommerfeld equation in the Galerkin expansion, found that the flow structures corresponding to the largest energy growth are toroidal vortex tubes. They are stretched by the shear stress of the mean flow so that a maximum energy growth occurs initially. The flow perturbation subsequently decays in time owing to viscous effects.

Experimental studies on the stability of pulsatile pipe flows are due to Gilbrech & Coombs (1963) and Sarpkaja (1966). Their investigations indicate that both the amplitude and frequency of the pulsation increase the critical Reynolds number as long as local flow reversal does not occur. Laminar to turbulent transition studies on pulsatile pipe flows were experimentally carried out by Yellin (1966), Ramaprian & Tu (1980), Shemer & Kit (1984), Shemer (1985) and Stettler & Hussain (1986). Yellin (1966) first introduced the concept of relaxation time to interpret the effects of a periodic component superposed onto the mean flow, and demonstrated that neither the mean nor the instantaneous Reynolds number provided a sufficient criterion for determining the laminar to turbulent transition boundary. He also showed, through the relaxation time concept, that slowly oscillating flows of large amplitude tend to suppress or destroy the turbulence downstream of the disturbance source. The study of Ramaprian & Tu (1980), dealing with transitional pipe flows at low Reynolds numbers, indicated that flow pulsations increase the critical Reynolds number. The occurrence and extent of laminarization was, however, found to depend on factors such as the intermittency of turbulent puffs in the mean quasi-steady flow and the frequency of oscillation. Shemer (1985) concluded that the transition phenomenon is primarily governed by the instantaneous Reynolds number. Stettler & Hussain (1986) performed an intensive experimental study and provided a three-dimensional map of stability–transition regimes, suggesting that transition in pipes is mainly associated

with plugs of turbulence that can grow or shrink in size. The measurements of Lodahl, Sumer & Fredosoe (1998) showed that the laminar to turbulent transition boundary is influenced by large values of the oscillating amplitude and frequency. The results of the DNS of Tuzi & Blondeaux (2008), obtained in a pipe characterized by small superficial wall imperfections, are in qualitative agreement with those of Lodahl *et al.* (1998). Discrepancies were attributed to the different level of flow perturbations present in the experimental apparatus with respect to those introduced in the numerical simulation by the wall imperfections.

There is a wealth of literature available on turbulent pulsating flows in circular pipes and channels, and many combinations of the governing parameters have been investigated (Ramaprian & Tu 1980, 1983; Tu & Ramaprian 1983; Shemer, Wygnanski & Kit 1985; Mao & Hanratty 1986; Tardu & Binder 1993; Mao & Hanratty 1994; Tardu, Binder & Blackwelder 1994; Lodahl *et al.* 1998; Scotti & Piomelli 2001; Zou, Liu & Lu 2006; Bhaganagar 2008; Blel *et al.* 2009; He & Jackson 2009).

Here, and in the following, by *current-dominated* regime we refer to flow conditions characterized by a small value of the oscillatory to mean velocity ratio (typically less than one), while in the *wave-dominated* case the above ratio is usually larger than one. Most, if not all, of the available contributions are concentrated on the current-dominated regime, while only a limited number of studies have dealt with the wave-dominated regime. This is unfortunate because both regimes enjoy specific flow features and are therefore equally interesting. Moreover, it has been experimentally shown by Lodahl *et al.* (1998) that, in a small region of the parameter space of the wave-dominated regime, the cycle-averaged wall shear stress may be smaller than that of the current component alone. In some cases this phenomenon may be quantitatively considerable, so that there are valid scientific motivations to further elaborate on the reasons for its genesis. In Lodahl *et al.* (1998) it is argued that the above behaviour is related to the occurrence of a reverse transition generated by the suppression of turbulence associated with the oscillatory mean shear, whenever the latter is in the laminar state. Results based on a large-eddy simulation (LES) (Manna & Vacca 2005, 2007) suggested that, in the above-mentioned cases, the averaged wall shear stress reduced while the turbulence survived at all times within the oscillating period.

The main objective of the present contribution is to provide, in the clean context offered by data from a spectrally accurate DNS, a detailed analysis of the previously described flow conditions. In the absence of any parametrization and/or measurement uncertainties, the complex interaction between the unsteady forcing and the fluctuating components of turbulence can be assessed.

On account of the flow periodicity, one might ask whether it should be analysed by time- and space-averaged statistics or by considering its phase-dependent dynamics. In the authors' opinion, both problems are relevant, and they certainly deserve an accurate investigation. Nevertheless, since there are several aspects of the mean flow that are not yet fully understood (like the already mentioned anomalous behaviour of cycle-averaged wall shear stress of the combined flow), it seems wise to perform the study of the time- and space-averaged flow before investigating the phase-dependent dynamics. Indeed, it will be shown that the first kind of analysis yields interesting and counterintuitive results that will be used as a springboard to analyse the phase-averaged statistics in a forthcoming paper.

This paper is organized as follows. In § 2 the flow problem is formulated and the relevant dimensionless parameters detailed. The numerical method and the computational aspects are described in § 3, while § 4 analyses the time- and space-averaged statistics of the first- and second-order moments, vorticity fluctuations and

Reynolds stress budgets. Conclusions are drawn in § 5. At the end of the paper an Appendix is given with the analysis of the invariants of the Reynolds stress and vorticity anisotropy tensors that further confirms the findings of § 4.

2. Problem formulation and background

We consider the incompressible pulsating flow through a circular pipe with diameter $D = 2R$ and axial length L_z driven by a time-varying harmonic body force of prescribed mean, amplitude and frequency. The resulting flow is characterized by a volume-averaged velocity consisting of a steady component U_b and a harmonically time-varying one, with amplitude U_o and pulsation $\omega = 2\pi/T$, T being the oscillation period. The forcing term is designed so that appropriate values of the dimensionless governing parameters are achieved. Pulsating flows are fully characterized by three dimensionless parameters, and one of the first choices is due to Yellin (1966):

$$Re_b = \frac{U_b D}{\nu}, \quad \Omega = \frac{R}{\delta}, \quad \beta = \frac{U_o}{U_b}, \tag{2.1}$$

where $\delta = \sqrt{2\nu/\omega}$ is the Stokes layer thickness, with ν the kinematic viscosity and Ω the Stokes number. Other triplets are also possible:

$$Re_b = \frac{U_b D}{\nu}, \quad \Omega_t = \frac{\omega D}{\overline{u}_\tau}, \quad \frac{U_m}{U_b}, \quad \text{Ramaprian \& Tu (1983)}, \tag{2.2}$$

$$Re_c = \frac{U_c D}{\nu}, \quad \omega^+ = \frac{2}{\delta^{+2}}, \quad \frac{U_m}{U_c}, \quad \text{Tardu \& Binder (1993)}, \tag{2.3}$$

$$Re_b, \quad Re_\omega = \frac{U_m^2}{(\omega\nu)}, \quad \frac{U_m}{U_b}, \quad \text{Lodahl } \textit{et al.} \text{ (1998)}, \tag{2.4}$$

with U_c the mean centreline velocity and U_m the maximum value of the oscillatory flow at the centre of the pipe, and the superscript $^+$ indicates the inner variables scaling, based on the space- and time-averaged friction velocity $\overline{u}_\tau$.

Nearly the entire literature has dealt with pulsating pipe or channel flows with β values less than one (current-dominated regime) (Ramaprian & Tu 1980, 1983; Tu & Ramaprian 1983; Shemer & Kit 1984; Shemer 1985; Mao & Hanratty 1986; Stettler & Hussain 1986; Tardu & Binder 1993; Tardu *et al.* 1994; Mao & Hanratty 1994; Scotti & Piomelli 2001; Bhaganagar 2008; He & Jackson 2009). In this regime, assuming a constant value of Re_b, there is some consensus that the driving frequency largely controls the flow features, and one possible classification is based on the turbulent Stokes number Ω_t (Ramaprian & Tu 1983). Interpreting Ω_t as the ratio of two characteristic length scales, namely the pipe radius R and the turbulent length $\delta_t = (2\nu_t/\omega)^{1/2}$, with ν_t the eddy viscosity in the outer layer assumed proportional to $\overline{u}_\tau R$, it may be argued that the turbulent Stokes number is a measure of the relative wall distance up to which unsteady vorticity penetrates the core flow. It is worth noting that Ω_t is considerably smaller than the laminar Stokes number for a given frequency, and the ratio between them (Ω_t/Ω) decreases as the Reynolds number increases, since it can be shown that the following relation holds (Ramaprian & Tu 1983):

$$\Omega_t = 8\frac{\Omega^2}{Re_\tau}, \tag{2.5}$$

with $Re_\tau = u_\tau D/\nu$.

Following Ramaprian & Tu (1983) five main regimes can be defined based on the value of Ω_t. In the type I or *quasi-steady* regime ($\Omega_t \leqslant 10^{-1}$), the flow behaves as a steady flow and there will be neither velocity overshoot nor phase lag of the ensemble-averaged quantities compared to the steady values obtained with a corresponding time constant pressure gradient. The turbulent structure does change within the oscillating period, but it can be described as a sequence of steady states, since at all times turbulence can relax to the local (in time) equilibrium.

The type II or *low-frequency* regime ($10^{-1} \leqslant \Omega_t \leqslant 1$) exhibits appreciable differences from the quasi-steady behaviour all across the pipe diameter, although the time mean flow will not be significantly different from that obtained with a quasi-steady analysis. The turbulence structure is not modified by the flow unsteadiness and it remains quasi-steady since the oscillation frequency f does not interact with the characteristic turbulent bursting frequency f_{burst}. This issue has been investigated by Mizuchina, Maruyama & Shiozaki (1973), who provided for the lower, mean and upper values of the bursting frequency approximate power-law correlations, in a moderate Reynolds number range.

The type III or *intermediate-frequency* regime ($1 \leqslant \Omega_t < 10$) is characterized by some interaction between the imposed unsteadiness and the turbulent structure. The latter will be affected, the changes being more pronounced as the oscillation frequency is increased. Also the turbulent equilibrium conditions will break down during part of the cycle and, as for the previous two regimes, the time mean flow does not significantly differ from the quasi-steady one, especially at the low end of the frequencies.

In the type IV or *high-frequency* regime ($\Omega_t \sim O(10)$ or higher), the imposed oscillation strongly interacts with the turbulent bursting process at the wall, and the turbulent structure is substantially altered. The time mean radial distribution of all quantities will differ from the corresponding quasi-steady one, sometimes through the appearance of inflection points in the near-wall region. Time-varying flow quantities will undergo significant changes in a near-wall thin layer while a solid-body-like oscillation condition will occur elsewhere. The turbulent structure will exhibit a remarkable departure from the equilibrium conditions in a small fraction of the pipe radius close to the wall, while it remains practically frozen in the outer part of the shear layer, where it shows an essentially flat streamwise velocity profile.

For $\Omega_t \sim 10^2$ (*rapid oscillation* or type V regime), the interaction between the imposed oscillation and the turbulent structure will be very strong, although confined to a very thin near-wall layer. Very little information is available in this regime.

A somewhat different route was proposed by Ronneberger & Ahrens (1977) and Binder & Kueny (1981), who introduced the so-called Stokes–Reynolds number δ^+ as the leading controlling dimensionless parameter. As discussed in detail in Tardu & Binder (1993), the δ^+ parameter defines the boundary above which the shear wave generated at the wall reaches the asymptotic outer value before turbulence can play an appreciable role in the momentum transfer. This is the so-called *high-frequency* regime occurring for $\delta^+ < 10$. The experiments of Tardu & Binder (1993) have shown a progressive departure from the Stokes solution at larger values of δ^+. There is no contradiction between the regime definition of Ramaprian & Tu (1983) and that of Tardu & Binder (1993), since the $\delta^+ < 10$ boundary falls in the type IV regime previously recalled, provided that the Reynolds number Re_b is in the 10^4 to 5×10^4 range.

Another classification, based on the turbulent Stokes length δ_t^+, now defined in terms of an effective viscosity $\nu + \nu_t$,

$$\delta_t^+ = \frac{u_\tau}{\nu}\sqrt{\frac{2(\nu+\nu_t)}{\omega}}, \tag{2.6}$$

has been introduced by Scotti & Piomelli (2001). The authors used an eddy viscosity concept for ν_t ($\nu_t = \kappa u_\tau \delta_t$, κ being the von Kármán constant) to derive the following expression for the turbulent Stokes length:

$$\delta_t^+ = \delta^+\left(\frac{\kappa\delta^+}{2} + \sqrt{1+\left(\frac{\kappa\delta^+}{2}\right)^2}\right). \tag{2.7}$$

In the quasi-steady regime, occurring when $\delta_t^+ \gg R^+$ (R^+ being the pipe radius in wall units), the turbulence has time to relax to the local (in time) equilibrium (Binder, Tardu & Vezin 1995).

In the low-frequency regime, which occurs whenever $\delta_t^+ \sim R^+$, the entire flow is affected by the unsteadiness in the inner region of the flow. Production and dissipation may become out of phase with respect to each other, and, if β is large enough, relaminarization can occur.

For $\delta_t^+ < R^+/2$, the intermediate regime is defined, and in the region $y^+ > 2\delta_t^+$, y being the distance from the wall, turbulence is frozen and advected as a plug flow.

At high frequencies ($10 < \delta_t^+ < 20$), the Stokes layer thickness is comparable to or smaller than the viscous sublayer, so that accurate results from both experiments or simulations are difficult to collect. At even higher frequencies ($\delta_t^+ < 10$), we enter the very high-frequency regime, and there is experimental evidence indicating that the modulation of the fluctuation of the wall shear stress deviates from the Stokes value. A possible explanation relies on the occurrence of resonance conditions between the forcing and the coherent structure bursting frequencies. The available data seem to indicate a moderate consensus on this matter. Uncertainties may be attributed, among other reasons, to the Reynolds number and geometry dependence of the bursting frequency (Luchik & Tiederman 1987; Tardu & Binder 1993; Scotti & Piomelli 2001).

The studies discussed above refer to those cases characterized by values of β smaller than one, that is, an oscillating velocity smaller than the mean one. The available literature in the wave-dominated regime is rather limited; the only study we are aware of is that of Lodahl *et al.* (1998), whose experimental analysis covered a large part of the dimensionless parameter space (see table 1 and figure 1). The laminar to turbulent transition was shown to occur at a Reynolds number Re_b larger than the critical value in the combined flow case, depending on the (Re_ω, Ω) pair. The ensemble-averaged turbulent profiles behave differently for different regimes. The space- and time-averaged wall shear stress of the combined motion was found to be smaller than, equal to or larger than the steady current value alone. The increase in the wave-dominated regime when the oscillating component is in the turbulent state may reach a factor of four. A reduction may take place when the oscillating component is in the laminar regime. For a fixed oscillating frequency (with Ω larger than 10), the shape of the boundary separating laminar from turbulent conditions in the Re_b–Re_ω plane looks like a hook (see figures 1 and 6 of Lodahl *et al.* 1998). More specifically, superposing an oscillating component for $Re_b < Re_{b,tr}$, $Re_{b,tr}$ being the transitional value in the absence of oscillation ($Re_{b,tr} \sim 2300$), the flow remains laminar until Re_ω reaches the transitional value in the absence of current ($Re_{\omega,tr} \sim 10^5$). For $Re_b > Re_{b,tr}$,

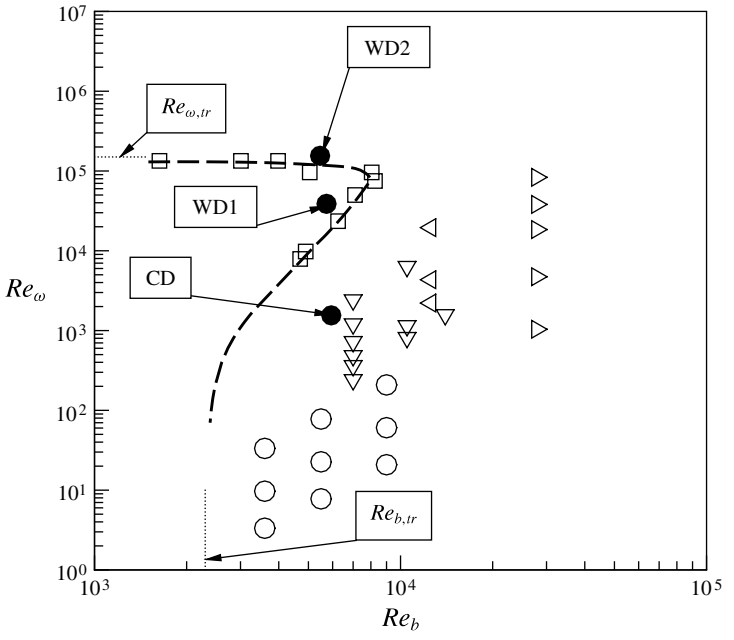

FIGURE 1. Laminar to turbulent transition boundary (dashed line) and available data for high-frequency regime ($\Omega \geqslant 10$). ◯, Shemer & Kit (1984); ▷, Tardu & Binder (1993); □, Lodahl *et al.* (1998); ◁, Scotti & Piomelli (2001); ▽, He & Jackson (2009); •, present calculations.

Author	Geometry	Methods	Re_b	Re_ω	Ω	β
Shemer & Kit (1984)	Pipe	Exp.	3.6×10^3 to 9.0×10^3	3.3 to 2.1×10^2	18–56	0.08
Tardu & Binder (1993)	Channel	Exp.	1.5×10^4	4.9×10^3 to 8.7×10^4	13–54	0.34–0.73
Lodahl *et al.* (1998)	Pipe	Exp.	0 to 1.6×10^5	7.9×10^3 to 1.3×10^5	25–53	3–30
Scotti & Piomelli (2001)	Channel	LES	1.3×10^4	2.3×10^3 to 2.0×10^4	25–80	0.76–0.86
He & Jackson (2009)	Pipe	Exp.	7.0×10^3 to 10.5×10^3	2.4×10^2 to 6.3×10^3	10–32	0.2–0.47

TABLE 1. Previous studies in the high-frequency regimes.

laminar conditions can only occur if $Re_{\omega 1} < Re_\omega < Re_{\omega 2}$; the difference between $Re_{\omega 2}$ and $Re_{\omega 1}$ reduces when Re_b increases, and vanishes at $Re_b/Re_{b,tr} \sim 3.5$ with $Re_\omega/Re_{\omega,tr} \sim 0.7$. As the oscillation frequency is reduced, the hook shape of the boundary tends to disappear, and for $\Omega \sim 3$ a nearly square boundary shape is observed.

The cases available in the literature, reported in figure 1, show that no investigations were carried out in the neighbourhood of the region inside which a reverse transition process occurs (Lodahl *et al.* 1998). This is the main motivation for the present

Acronym	Re_b	Re_ω	Ω	β
CD	5939	1.6×10^3	53.0	1.0
WD1	5730	3.9×10^4	53.0	5.0
WD2	5460	1.6×10^5	53.0	10.6

TABLE 2. Run matrix.

paper, and specifically we wish to investigate, via DNS, the three flow conditions identified by the (Re_ω, Re_b) pairs defined in table 2. To the authors' knowledge this is the first time in which the flow has been analysed keeping Re_b (approximately) constant and varying Re_ω for a range wide enough to cross all the boundaries of the laminar–turbulent transitions curve.

All pulsating cases are characterized by the same Stokes layer thickness, that is, by a constant Ω value. Conversely, for nearly equal bulk Reynolds number, the oscillating Reynolds number Re_ω is increased by a factor 100, crossing both the lower and upper branches of the hook-like boundary (see figure 1). The increase of Re_ω can be interpreted as a a direct consequence of the increase in the oscillating velocity component, since the forcing frequency is kept unchanged. By doing so, we investigate both wave- and current-dominated flow conditions. For the sake of comparison, a steady simulation has also been carried out at $Re_b = 5920$ and it is denoted by ST.

3. Numerical method and computational set-up

The governing equations are the three-dimensional incompressible Navier–Stokes equations, whose dimensional form is

$$\frac{\partial \boldsymbol{u}}{\partial t} + \mathscr{N}(\boldsymbol{u}) = -\boldsymbol{\nabla} P + \mathscr{L}(\boldsymbol{u}) + \mathscr{S}, \tag{3.1}$$

with

$$\boldsymbol{\nabla} \cdot \boldsymbol{u} = 0, \tag{3.2}$$

where $P = p/\rho$, p and ρ being the pressure and the fluid density, respectively. Equations (3.1) and (3.2) have been integrated in a circular pipe of diameter D and length L_z. The velocity components of $\boldsymbol{u}$ in cylindrical coordinates are $\boldsymbol{u} = (u_z, u_r, u_\theta)^t = (u, v, w)^t$, in the axial (streamwise), radial and azimuthal directions, respectively. The differential operators $\mathscr{N}(\boldsymbol{u}) = (\boldsymbol{u} \cdot \boldsymbol{\nabla})\boldsymbol{u}$ and $\mathscr{L}(\boldsymbol{u}) = \nu \Delta \boldsymbol{u}$ represent the convective and diffusive terms. In the present flow, the source term $\mathscr{S}$ is given by $\mathscr{S} = (S_z, 0, 0)^t$ with

$$S_z = S_0[1 + \alpha \cos(\omega t)]. \tag{3.3}$$

The triplet (S_0, α, ω) has been assigned so as to obtain the dimensional parameters given in table 2. Owing to the nonlinear dependence of the velocity field upon the body force $\mathscr{S}$, it is impossible to specify *a priori* a triplet yielding a precise value of the dimensionless parameters appearing in table 2. Furthermore, the reduction of the time-averaged wall shear stress, which may be interpreted as a mean flow rate increase for a fixed value of (S_0, α, ω), makes the problem set-up even more complex. In the present study, the actual mean flow rate and the associated value of β have been obtained by modifying the initial provisional values estimated via the theoretical

Blasius correlations. This explains the slight scatter in the dimensionless parameters in table 2.

The numerical solution of (3.1) and (3.2) has been carried out using a pressure correction scheme and a pseudo-spectral multi-domain technique. In what follows we only briefly summarize the solution technique – additional details can be found in Manna & Vacca (2009). A full description of the numerical method is available in Manna & Vacca (1999). We uncouple the velocity field and the pressure at each time step using a standard time splitting technique (Van Kan 1986) and, to enhance the stability restriction related to the near-wall gradients, we discretize implicitly the diffusive terms in the prediction step, while the convective part, written in skew-symmetric form, and the source term are treated explicitly. Since we deal with unsteady flows, we require overall second-order time accuracy, that is, a Crank–Nicolson scheme for the viscous term and an Adams–Bashforth scheme for the remaining ones. The variables and the derivatives appearing in the differential operators of (3.1) and (3.2) are represented in truncated Fourier series in the axial and azimuthal homogeneous directions, while Chebyshev expansion is used in the inhomogeneous radial one. The axis singularity is dealt with using a special innovative procedure based on the use of Gauss–Radau collocation points, which automatically satisfies the pole condition. The multi-domain technique based on patching interfaces provides additional flexibility, in terms of both computational efficiency and near-wall resolution. The elliptic kernel enjoys the efficiency of an analytic expansion of the harmonic extension. Further details about the accuracy and efficiency of the method, together with several benchmarks for the validation of the numerical procedure, are given in Manna & Vacca (1999).

Numerical results have been obtained in a domain whose dimensionless axial length $l_z = L_z/R$ has been set equal to 12 for the steady (ST) and current-dominated (CD) simulations and to 28 for the wave-dominated ones (WD1 and WD2), in order to account for the elongation of the near-wall coherent structures, which usually takes place when the wall shear stress for identical Reynolds number reduces (Orlandi & Fatica 1997; Quadrio & Sibilla 2000). *A posteriori* analysis of the computed data has shown that the adopted pipe length is sufficient for the streamwise velocity autocorrelation function to drop to zero (figure 2). Indeed, in the WD2 case, all curves decrease less rapidly than in the other cases, and the rate of decay of the autocorrelation for the radial velocity component becomes the slowest for $y^+ \geqslant 350$. The reason for this slow decay is well evidenced by the comparison of figures 3–5, where instantaneous snapshots, in inner coordinates, of the radial velocity component show the streamwise elongation of the near-wall turbulent structures.

The computational domain has been radially split into seven subdomains ($N_{sub} = 7$), each having $N_r = 12$ and $N_\theta = 192$ modes in the radial and azimuthal directions, respectively. The number of Fourier modes in the axial direction has been set to $N_z = 192$ in the steady and current-dominated simulations. To preserve the resolution in the axial direction, the number of modes in the wave-dominated regime has been increased to $N_z = 450$. The radial distribution of subdomain widths in the radial direction has been devised to enhance the wall-layer resolution; the radial width distribution of the seven subdomains, given in percentage of the radius, is as follows: 2, 3, 5, 8, 13, 24, 45 %. Using the computed values of the space- and time-averaged friction velocity $\overline{u}_\tau = \sqrt{S_0 R/2}$, in table 3 we give the relevant details associated with the spatial discretization, whose controlling parameters are also provided.

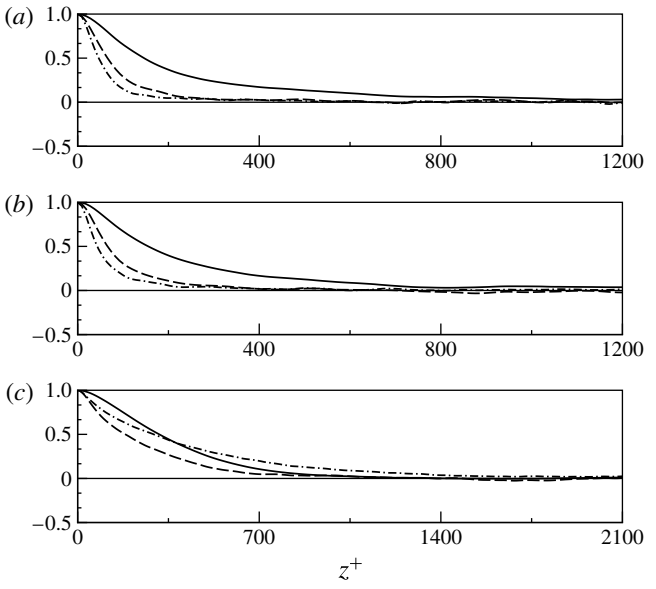

FIGURE 2. Velocity spatial correlations in the streamwise direction for (*a*) ST case, (*b*) CD case and (*c*) WD2 case. ——, streamwise component; — · —, radial component; – – – –, azimuthal component. All the correlations have been computed at a distance of $y^+ = 6$ from the wall.

Acronym	N_{sub} $(N_z \times N_r \times N_\theta)$	l_z^+	Δz^+	$(R\Delta\theta)^+$	$y_w^+ = \Delta r_{min}^+$
ST	7 $(192 \times 12 \times 192)$	2398	9.4	6.6	0.081
CD	7 $(192 \times 12 \times 192)$	2359	9.3	6.5	0.080
WD1	7 $(450 \times 12 \times 192)$	3008	6.7	3.5	0.044
WD2	7 $(450 \times 12 \times 192)$	4479	10.0	5.3	0.065

TABLE 3. Computational domain grid parameters.

The grid resolution, comparable to that of Eggels *et al.* (1994), Orlandi & Fatica (1997) and Quadrio & Sibilla (2000), satisfies the severe DNS requirements and ensures the quality of the collected data.

The ST, CD and WD2 cases have been obtained starting from the LES fields of Manna & Vacca (2007), which have been interpolated on denser grids. For the WD2 case, a mapping procedure through a set of intermediate grids of appropriate sizes has been applied to account for the necessity to increase the computational domain length. The procedure used to obtain the WD1 case is described later.

Numerical results for the statistically steady case have been obtained by processing 50 statistically independent fields separated in time by 0.1 dimensionless units $D/\overline{u}_\tau$. In order to assess the convergence of the results, some statistics have been computed using only the first half of the samples (spanning only $2.5D/u_\tau$ time units) and the results for the root mean square (r.m.s.) velocity fluctuations and the Reynolds stresses have shown a maximum deviation of 3 % with respect to the same quantities computed using the whole dataset (covering $5D/u_\tau$ time units). A similar quality of agreement

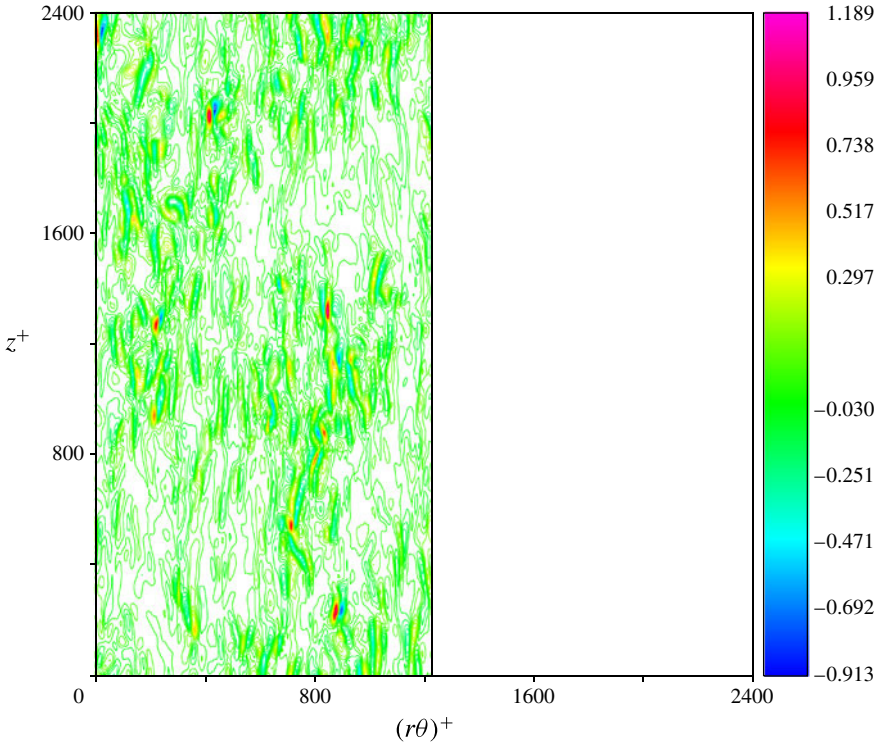

FIGURE 3. Instantaneous snapshot in inner coordinates of radial velocity component contours for the ST case at a distance of $y^+ = 6$ from the wall.

has been observed when the spacing of the samples was doubled to $0.2D/u_\tau$. The data collection was started only once a constant time- and space-averaged wall shear stress and a linear total shear stress radial distribution were achieved. All quantities are space-averaged in the homogeneous z and θ directions. In the pulsating cases a total of 50 cycles have been collected, each consisting of eight fields evenly spaced over the period.

Representative figures for the CPU requirement of the runs are given for the CD case: the simulation required slightly less than 1 GB of RAM memory and, using a $\Delta t^+ = 1.7 \times 10^{-5}$, it needed about 150 single-core equivalent hours per period.

In what follows, we shall denote with an overline the space- and time-averaged quantities, with a tilde the phase- and space-averaged quantities, and with a prime the perturbation from their time averages.

Table 4 compares several mean flow properties for the steady pipe flow with those reported by Eggels *et al.* (1994), Orlandi & Fatica (1997) and Quadrio & Sibilla (2000). The displacement (δ^*) and the momentum (θ^*) thicknesses and the shape factor (H) are defined as

$$\delta^*(D-\delta^*) = 2\int_0^R \left(1-\frac{\overline{u}(r)}{U_c}\right) r\,\mathrm{d}r, \tag{3.4a}$$

$$\theta^*(D-\theta^*) = 2\int_0^R \left(1-\frac{\overline{u}(r)}{U_c}\right)\frac{\overline{u}(r)}{U_c} r\,\mathrm{d}r, \quad H=\frac{\delta^*}{\theta^*}. \tag{3.4b}$$

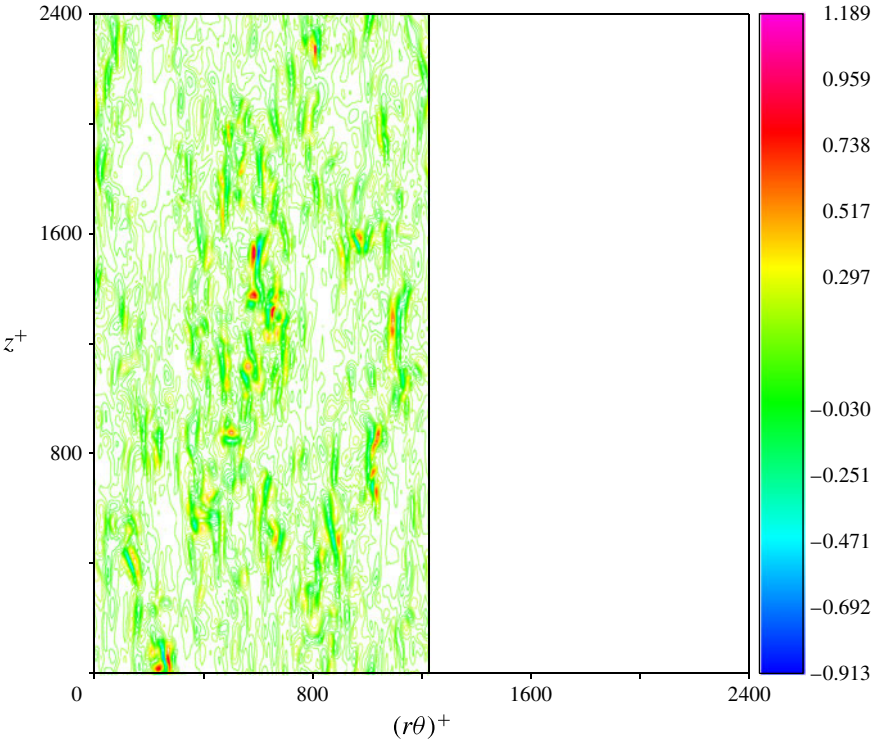

FIGURE 4. Instantaneous snapshot in inner coordinates of radial velocity component contours for the CD case at a distance of $y^+ = 6$ from the wall and at three-quarters of the oscillating period.

The agreement between the DNS data and the experiments (obtained using a single-wire anemometer) is good. In particular, the percentage change of the skin friction coefficient with respect to the Blasius value $C_f^B = 0.079Re^{-0.25}$ is within one per cent, for all but one case.

Figure 6 compares the mean velocity profile and the turbulent intensities in inner coordinates with those of Eggels *et al.* (1994). Once again, the agreement is very good, especially considering the differences in the Reynolds number ($Re = 5300$ in Eggels *et al.* (1994) versus $Re = 5920$ in the present study) and the streamwise length ($l_z = 10$ versus $l_z = 12$) of the domain. At these low Reynolds numbers, the deviation of the velocity profile from the theoretical distribution $\overline{u}^+ = (1/\kappa)\ln(y^+) + B$ (with $\kappa = 0.41$ and $B = 5.5$) is expected and is similar to that observed in several experiments and simulations (Barenblatt 1993*a*,*b*; Eggels *et al.* 1994; Orlandi & Fatica 1997; Zagarola & Smits 1998).

4. Results

We begin the analysis of the pulsating cases by comparing some global quantities with the steady flow counterparts (table 5). Let us first discuss the WD1 case, which falls inside the hook-like line in the Re_c–Re_ω plane of figure 1. This line defines the region in which the experiments of Lodahl *et al.* (1998) predict the occurrence of laminar flow conditions at a bulk Reynolds number larger than $Re_{b,tr}$.

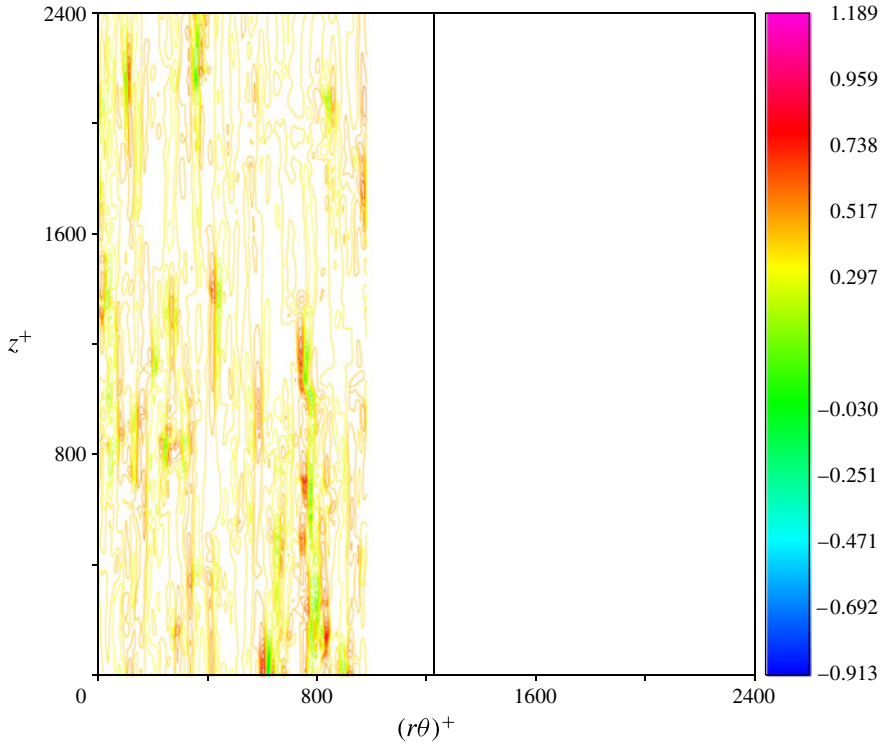

FIGURE 5. Instantaneous snapshot in inner coordinates of radial velocity component contours for the WD2 case at a distance of $y^+ = 6$ from the wall and at three-quarters of the oscillating period.

	Present	Eggels *et al.* (1994)		Orlandi & Fatica (1997)	Quadrio & Sibilla (2000)
	DNS	Exp.	DNS	DNS	DNS
U_c/U_b	1.30	1.31	1.31	1.31	1.31
$U_b/\overline{u}_\tau$	14.81	14.73	14.79	14.41	14.24
$U_c/\overline{u}_\tau$	19.24	19.40	19.31	18.87	18.63
$(C_f - C_f^B)/C_f^B$ (%)	1.24	0.52	−0.42	1.99	4.42
Re_c	7689	7350	6950	6400	6419
Re	5920	5600	5300	4900	4900
Re_τ	200	190	180	170	172
δ^*/R	0.123	0.128	0.127	—	—
θ^*/R	0.068	0.070	0.078	—	—
$H = \delta^*/\theta^*$	1.80	1.83	1.86	—	—

TABLE 4. Global mean properties for steady turbulent flow.

The data reported in table 5 are in excellent agreement with the laminar values (e.g. $\delta^*/R = 0.293$, $\theta^*/R = 0.087$, $H = 3.36$), therefore supporting the experimental findings of Lodahl *et al.* (1998). It should be noted that the WD1 case has been obtained

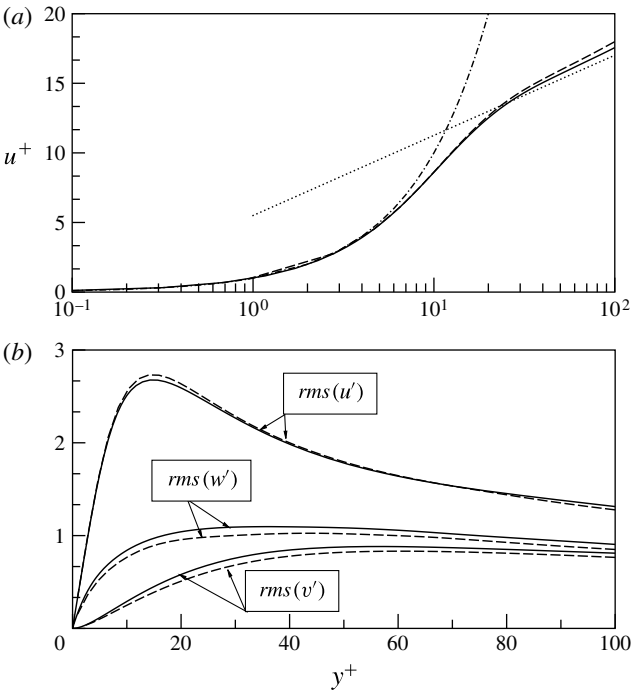

FIGURE 6. (*a*) Mean velocity profiles and (*b*) mean turbulent intensities. ——, present results; – – – –, Eggels *et al.* (1994); · · · · · ·, $\overline{u}^+ = (1/0.41)\ln(y^+) + 5.5$; — · —, $\overline{u}^+ = y^+$. The coordinate y is defined as $y = 1 - r/R$ and y^+ is the same quantity expressed in wall units.

starting from a field of the WD2 case (therefore turbulent) and allowing it to relax to the new dynamic condition. In more detail, applying a procedure similar to the one used to obtain CD and WD2, the parameter α of (3.3) appearing in the forcing term $\mathscr{S}$ of (3.1) has been modified so that the Re_c–Re_ω pair would fall in the laminar region of figure 1. After a long transient (of several hundred oscillating periods) characterized by a monotonic decrease of the volume-averaged turbulent kinetic energy, the large- and small-scale structures disappeared and the flow relaminarized. Looking at table 5, we note for the CD and WD2 cases that, while the ratio between the centreline and bulk velocities U_c/U_b is very close to the value for the steady pipe flow, the quantities $U_c/\overline{u}_\tau$ and $U_b/\overline{u}_\tau$ are seen to increase from 2 to 16 % in the CD and WD2 cases, respectively. This phenomenon reflects the reduction of the space- and time-averaged wall shear stress, which reaches a remarkable -25 %, compared to either Blasius or Colebrook–White values, in the WD2 case. In the CD simulation, a similar tendency is also observed. The displacement and momentum thicknesses show negligible variations in the CD case, while appreciable changes occur in the WD2 case, and this is reflected by the shape factor H that increases by about 11 %. Recalling that the laminar value is 3.36, we obtain confirmation of the occurrence of some wall shear stress reduction as well as modification of the shape of the velocity profile. If we consider the effect of the oscillating velocity modulation to be negligible and apply the criterion based on turbulent Stokes number Ω_t (Ramaprian & Tu 1983) to characterize the flow conditions CD and WD2, we could conclude that both simulations are very close to the type V regime (i.e. *rapid oscillation* regime, $\Omega_t^+ \sim 100$), while according

Acronym	ST	CD	WD1	WD2
U_c/U_b	1.30	1.30	1.99	1.32
$U_b/\overline{u}_\tau$	14.81	15.10	26.67	17.07
$U_c/\overline{u}_\tau$	19.24	19.65	53.11	22.55
$(C_f - C_f^B)/C_f^B$ (%)	1.24	−2.59	−69.02	−25.29
$(\lambda - \lambda^{CW})/\lambda^{CW}$ (%)	2.34	−1.53	−68.71	−24.67
Re_c	7689	7728	11412	7183
Re	5920	5939	5730	5460
Re_τ	200	197	107	160
δ^*/R	0.123	0.123	0.291	0.128
θ^*/R	0.068	0.068	0.087	0.064
H	1.80	1.81	3.34	2.00
U_m/U_b	—	0.99	5.15	10.81
δ^+	—	3.71	2.03	3.02
δ_t^+	—	7.48	3.04	5.42
Ω_t	—	57.1	104.5	70.2

TABLE 5. Mean flow properties.

to Tardu & Binder (1993) both cases belong to the very high-frequency regime (i.e. $\delta^+ < 10$). Adopting the criterion of the turbulent penetration length δ_t^+ of Scotti & Piomelli (2001), both simulations fall into the *very high-frequency* regime (i.e. $\delta_t^+ < 10$).

The radial distribution of the time-averaged mean velocity is reported in inner coordinates in figure 7, for all β values. As already discussed earlier, the flow in the WD1 case is laminar, with a parabolic shape, and this can be clearly appreciated by the near-wall velocity profile of figure 7. In the current-dominated case, the profile essentially collapses onto that of the steady distribution. This is a non-trivial result, since the amplitude of the velocity oscillation is such that flow reversal occurs close to the wall. The somewhat surprising insensitivity of the mean flow profile to the imposed oscillations, in the case $\beta < 1$, is controversial; in fact, the experimental data of Tu & Ramaprian (1983) (i.e. $\beta = 0.15$, $f^+ = 1.0 \times 10^{-3}$ and $\beta = 0.64$, $f^+ = 1.4 \times 10^{-4}$) show that, for oscillating frequencies comparable to or larger than the turbulent bursting frequency ($f^+_{burst} = 3.3 \times 10^{-3}$; Blackwelder & Haritonidis 1983), a definite deviation of the time-averaged distribution from the steady one occurs. Moreover, for frequencies and amplitudes within that range, the time-averaged velocity obtained by the quasi-steady approximation is nearly indistinguishable from the steady one. More recently, both experimental (Brereton, Reynolds & Jayaraman 1990; Tardu *et al.* 1994) and numerical (Scotti & Piomelli 2001) data have suggested the insensitivity of the mean flow to the imposed oscillation regardless of the closeness to the bursting frequency. While the data of Brereton *et al.* (1990) and Scotti & Piomelli (2001) closely follow the logarithmic distribution, those of Tardu *et al.* (1994) show a consistent upward shift in the wall layer, regardless of the oscillating frequency.

In the present simulations, the oscillating case with $\beta = 10.6$ still shows a logarithmic region with a slope $1/\kappa$ ($\kappa = 0.41$) that essentially equals the steady value, although an upward shift is observed. This shift, and the consequent increase of the viscous sublayer thickness, is typical of drag reducing flows (see e.g. Choi 1989; Quadrio & Sibilla 2000; Ptasinski *et al.* 2003).

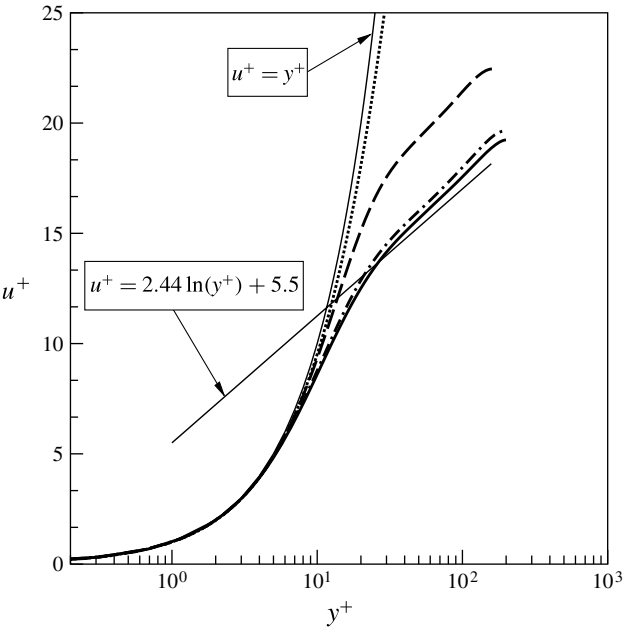

FIGURE 7. Mean velocity profiles. ——, ST case; — · —, CD case; · · · · · ·, WD1 case; – – – –, WD2 case.

Figure 8 shows, in inner coordinates, the radial distribution of the r.m.s. values of the fluctuating velocity components $rms(u')$, $rms(v')$ and $rms(w')$. The same figure reports the streamwise turbulent intensities for the channel geometry of Tardu *et al.* (1994) (experiments: at $Re_c = 1.70 \times 10^4$, $\delta^+ = 8.1$ and $U_m/U_c = 0.64$) and Scotti & Piomelli (2001) (LES: at $Re_c = 1.45 \times 10^4$, $\delta^+ = 4.4$ and $U_m/U_c = 0.75$), compared with the steady DNS data of Moser, Kim & Mansour (1999) (at $Re_c = 1.58 \times 10^4$). The data clearly show that, in the current-dominated very high-frequency regime, there is no effect of the forcing on the time-averaged diagonal components of the Reynolds stresses, independently of the geometry (pipe versus channel) and in a small envelope of the Reynolds number ($Re_c = 7.73 \times 10^3$ versus $Re_c = 1.58 \times 10^4$). This insensitivity in the very high-frequency regime has already been experimentally documented in channels (Tardu *et al.* 1994) and pipes (Hwang & Brereton 1991), while at lower frequencies a trend towards higher values can be observed (Tardu *et al.* 1994; Scotti & Piomelli 2001). As pointed out by Tardu *et al.* (1994), the insensitivity of the mean turbulence quantities in the high-frequency regime conflicts with the measurements of Mizushina, Maruyama & Hirasawa (1975) and Tu & Ramaprian (1983), the discrepancies being attributed to the occurrence of the already mentioned, though controversial, resonance condition between the oscillatory forcing and turbulent bursting frequency.

The above picture changes quite substantially in the $\beta = 10.6$ case. The streamwise turbulent intensity exceeds the steady value up to $y^+ \sim 60$, while the opposite happens elsewhere. Conversely, the radial and azimuthal components are reduced everywhere. Unfortunately, there are neither experimental nor numerical data with which to compare our results. Using outer scaling (results not shown), the uniform reduction of the radial and azimuthal components all across the pipe radius is confirmed, while

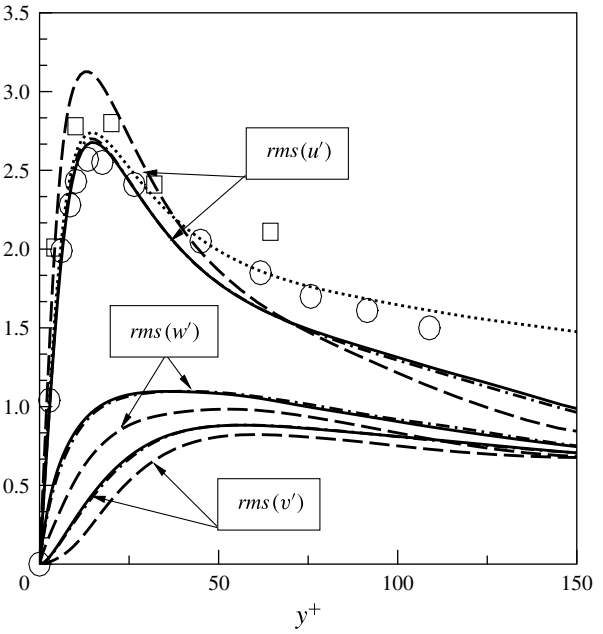

FIGURE 8. Mean turbulent intensities. ——, ST case; — · —, CD case; — · —, WD2 case. · · · · · ·, DNS channel data of Moser *et al.* (1999); ◯, LES channel data of Scotti & Piomelli (2001); □, experimental channel data of Tardu *et al.* (1994).

the streamwise intensity does not differ from the steady one up to $y \sim 0.3$ and reduces in the bulk. The difference between the two representations is a direct consequence of the wall shear stress reduction. The fact that the turbulent intensities have been altered all across the pipe radius is somewhat surprising in view of the tiny Stokes (turbulent) layer thickness $\delta = R/53$ ($\delta_t \sim R/30$).

Figure 9(*a*) presents the turbulent and viscous shear stresses, normalized by the wall friction velocity, in outer coordinates, while in figure 9(*b*) the percentage contribution of turbulent shear stress to the total one is detailed. As before, in the current-dominated simulation, neither viscous nor turbulent stresses differ appreciably from the steady distribution. Conversely, in the wave-dominated regime, important changes are visible. In particular, the dimensionless distance from the wall, where the viscous stress equals the turbulent one, increases from $\ell_c \sim 0.065$ to $\ell_c \sim 0.12$. For comparison, in the same figure twice the turbulent Stokes length $\ell_t = 2\delta_t = 2\delta_t^+/Re_\tau$ is shown for the wave-dominated case ($\ell_t = 0.068$). The turbulent Stokes length for the current-dominated case is not reported, since it differs slightly from the WD2 value ($\ell_t = 0.076$). It is worth noting that the turbulent penetration length ℓ_t nearly coincides with ℓ_c of the CD case, while ℓ_c exceeds ℓ_t by nearly a factor of 1.8 in the WD2 case. In other words, the fractional contribution of the turbulent stress to the total one is smaller than 16 % at $y = \ell_t$. Indeed, we are witnessing a thickening of the viscous sublayer and associated buffer layer modification, which was already pointed out while discussing the mean velocity profiles. The expected decoupling between the inner ($y < \ell_t$) and outer layers, representing a characteristic feature of the very high-frequency regime, does not occur in the presence of large-amplitude oscillations,

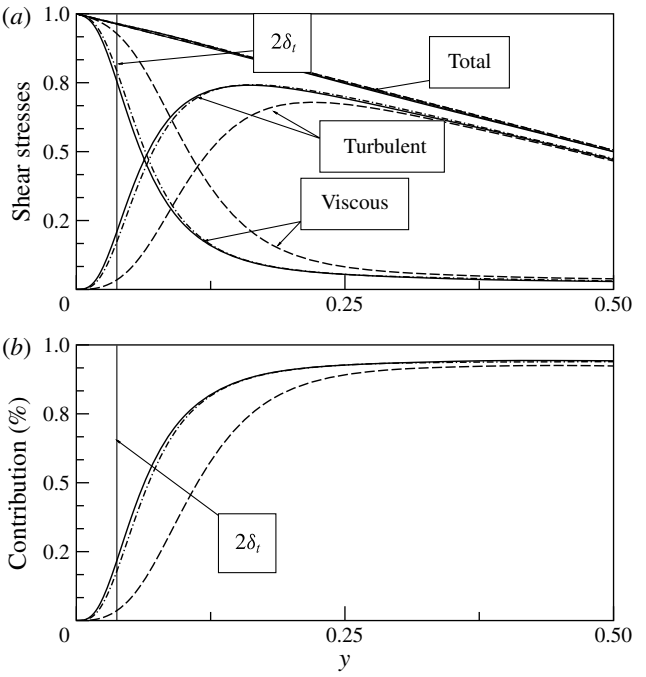

FIGURE 9. (*a*) Viscous and turbulent shear stresses and (*b*) percentage contribution of turbulent shear stress to the total one. ——, ST case; — · —, CD case; – – – –, WD2 case.

since the outer layer is not frozen and feels the effects of the unsteady forcing up to $y \sim 0.3$.

Figure 10 shows the structure parameter (SP), i.e. the ratio of the shear stress to twice the turbulent kinetic energy K. Recalling that, under the equilibrium assumption, this parameter equals 0.15, we note that both ST and CD simulations show a quasi-equilibrium layer of ∼70 wall units starting from $y^+ \sim 70$, using an uncertainty band of ±10 %. These data agree with the high-frequency results of Scotti & Piomelli (2001), also obtained in the current-dominated regime. At higher amplitudes, the structure parameter reduces everywhere. Adopting the aforementioned 10 % criterion, the near-equilibrium layer shifts towards the wall ($y^+ \sim 60$) and reduces in size (∼20 wall units).

In figure 11 vorticity fluctuations (enstrophy) normalized by the mean wall shear stress $\omega_i' \nu / \overline{u}_\tau^2$ are shown. In the steady and current-dominated simulations, minor differences in the azimuthal vorticity component appear for $y^+ < 20$. For $y^+ > 50$, all components collapse onto a single curve. The streamwise component exhibits a local maximum and minimum, a fact that has been attributed to the streamwise vortices in the wall region (Moser & Moin 1984). The location of the local maximum (minimum) corresponds, statistically, to the average location of the centre (edge) of the streamwise vortices. In agreement with the DNS data of Kim, Moin & Moser (1987), the average locations of the centre and the edge of the streamwise vortices are $y^+_{\omega_z,max} = 20$ and $y^+_{\omega_z,min} = 5$. The corresponding strengths are 0.15 and 0.10 $\overline{u}_\tau^2/\nu$. In the wave-dominated case, again the vorticity distributions nearly collapse onto a single curve for $y^+ > 50$, while in the wall region remarkable differences exist.

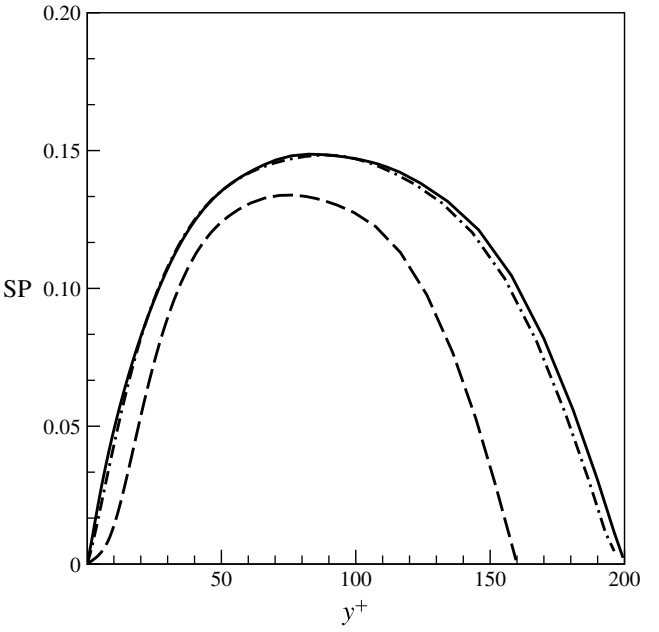

FIGURE 10. Structure parameter (SP). For curves, see figure 9.

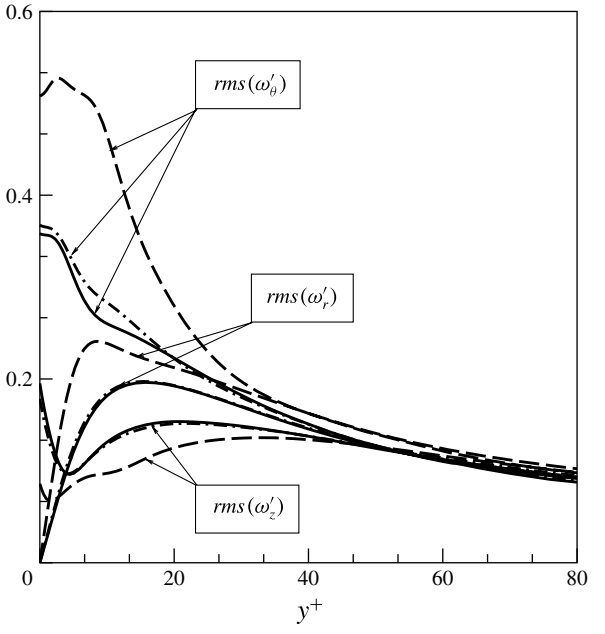

FIGURE 11. R.m.s. vorticity fluctuations. For curves, see figure 9.

In particular, while the azimuthal and radial components exceed the corresponding CD values, the streamwise one shows some reduction and new extrema locations,

Acronym	$\mathbb{P}_{cur}$	$\mathbb{P}_{osc}$	$\mathbb{P}_{tot}$
ST	0.0091	—	0.0091
CD	0.0088	0.0175	0.0263
WD1	0.0028	0.4836	0.4864
WD2	0.0068	2.2386	2.2454

TABLE 6. Dimensionless cycle-averaged power.

i.e. $y^+_{\omega_z,min} = 1.5$ and $y^+_{\omega_z,max} = 32$. The increase in the ω'_θ and ω'_r distributions is an outcome of the adopted inner scaling representation, and more specifically of the wall friction reduction discussed earlier. Outer scaling indicates a reduction of all vorticity components. The wall value of ω'_z halves with β, a phenomenon that can be associated with the modification in the splatting mechanism discussed later.

The above-mentioned change in the positions of the streamwise vorticity extrema suggests a nearly double radial extent of the streamwise vortices, a fact that entails a reduction in the turbulence production mechanism as dictated by the near-wall streaks dynamics. Outer scaling confirms the above results.

When analysing the dimensionless power required to drive the overall flow,

$$\mathbb{P}(t) = \frac{\rho S_z(t) L_z \sigma u_b(t)}{\rho u_b^3 \sigma} = S_z(t) L_z u_b(t), \tag{4.1}$$

σ being the pipe cross-sectional area, it turns out that the cycle-averaged values increase with β, irrespective of the flow state (laminar, transitional or turbulent) characterizing the current part. In table 6 the quantities

$$\mathbb{P}_{tot} = \overline{\mathbb{P}(t)} = \mathbb{P}_{cur} + \mathbb{P}_{osc} = \frac{S_0 L_z}{U_b^2} + \frac{S_0 L_z}{U_b^3} \overline{\cos(\omega t)(u_b(t) - U_b)} \tag{4.2}$$

are given for all cases.

While $\mathbb{P}_{cur}$ reduces with β in the turbulent cases (CD and WD2), reaching its minimum when the reverse transition process is completed (WD1), the oscillating part overwhelms the corresponding current value, so that the trend of their sum reflects the oscillating one. In the present set-up, the oscillating part increases nearly quadratically with β. Indeed, in all cases, the oscillating flow obeys the Stokes solution

$$U_s = U_m \,\mathrm{Re}\left[\mathrm{i}\left(\frac{\mathrm{J}_0(i^{3/2}\sqrt{2}r/\delta)}{\mathrm{J}_0(i^{3/2}\sqrt{2}\Omega)} - 1\right)\mathrm{e}^{\mathrm{i}\omega t}\right], \tag{4.3}$$

where J_0 is the Bessel function of the first kind of order zero (Abramowitz & Stegun 1972), i is the imaginary unit and $\mathrm{Re}[\,\cdot\,]$ is the real part of the argument. This is clearly shown by figure 12, in which the amplitude and the phase of the streamwise velocity component are compared with the Stokes solution (4.3). The amplitude and phase of the computed data are obtained by selecting the first mode of the n-truncated Fourier series in the time domain:

$$\langle u \rangle = \overline{u} + A_{\tilde{u}} \cos(\omega t + \Phi_{\tilde{u}}) + \sum_{i=2}^{n} A_{\tilde{u}i} \cos(\omega t + \Phi_{\tilde{u}i}). \tag{4.4}$$

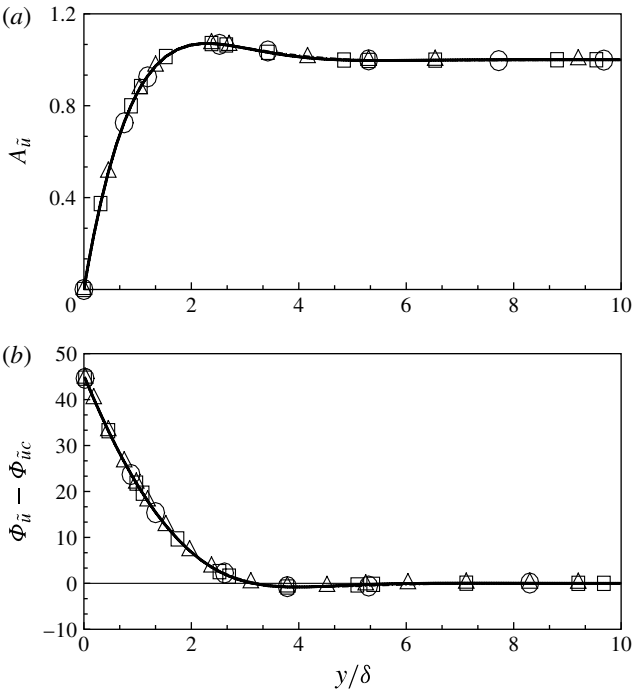

FIGURE 12. Streamwise velocity profiles, showing (*a*) amplitude ($A_{\tilde{u}}$) and (*b*) phase lag with respect to the centreline value ($\Phi_{\tilde{u}} - \Phi_{\tilde{u}c}$). ——, Stokes solution (4.3); — · — and ◯, CD case; · · · · · · and □, WD1 case; – – – – and △, WD2 case.

This shows that the increase of the oscillation amplitude for a given frequency has a definite impact on the features of the current flow; conversely, there is no effect on the velocity distribution of the oscillating part, i.e. the flow appears to be one way coupled. While the first result has already been documented both experimentally (Tardu *et al.* 1994) and numerically (Scotti & Piomelli 2001), to the best of our knowledge the latter is new. In a slightly different flow, similar findings have been reported by Quadrio, Ricco & Viotti (2009) and Viotti, Quadrio & Luchini (2009).

With the idea of characterizing the organized structures associated with the bursting events, we present in figure 13 the contribution to the Reynolds stress (mainly $\overline{u'v'}$) from each quadrant as a function of the wall distance in inner coordinates (Wallace, Ecklmann & Brodkey 1972; Willmarth & Lu 1972), for all cases. The sign of the radial component has been changed, in order to use the customary terminology to refer to ejections as events pertaining to the second quadrant, and sweeps to the fourth one. The data of the $\beta = 1$ case confirm the dominance of the ejection events (second quadrant) away from the wall and of the sweep events close to the wall (fourth quadrant, $y^+ \leqslant 15$) characterizing the steady flow. In the WD2 case, the well-known dominance of the sweeps in the wall region is reduced, so that the contributions of the second and fourth quadrants to the shear stress are roughly the same (see figure 13*c*), while for $y^+ > 20$ no major differences with respect to the CD case are observed. It should be remarked that the magnitude of the quantities reported in figure 13 is not a direct measure of the intensity of each event, because they are normalized by the local turbulent shear stress, which in the WD2 case reduces considerably.

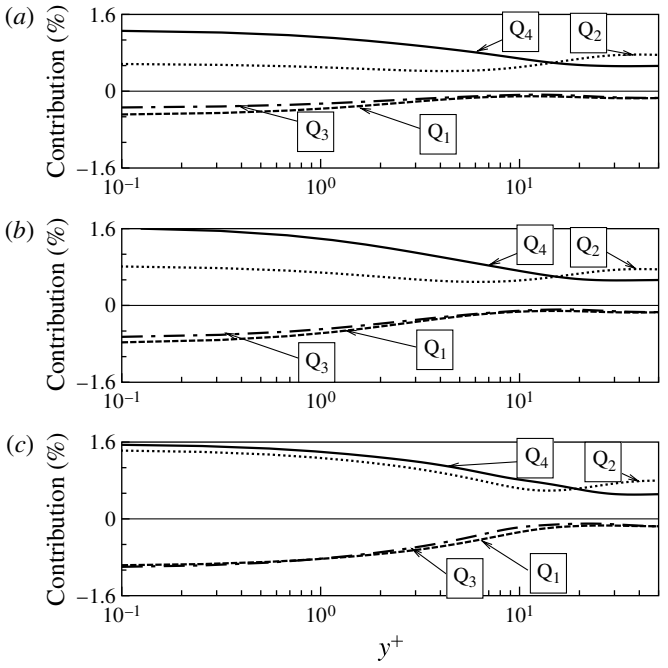

FIGURE 13. Quadrant analysis of velocity fluctuations. (*a*) ST case; (*b*) CD case; and (*c*) WD2 case.

In what follows we present the time-averaged transport equations for the normal stresses, which are formally written as

$$P + T + D + \Pi - \epsilon = 0, \tag{4.5}$$

where P, T, D, $-\epsilon$ and Π denote production, turbulent transport, viscous diffusion, dissipation rates and velocity pressure gradient, respectively. Incidentally, let us recall that the individual terms appearing in (4.5) come from the application of the time-averaging operator to the phase-locked quantities. They are given by the following:

$$\overline{u'^2}\text{-budget} \quad \underbrace{-2\overline{\langle u'v'\rangle}\frac{\mathrm{d}\langle u\rangle}{\mathrm{d}r}}_{P} \underbrace{-\frac{1}{r}\overline{\frac{\partial(ru'^2v')}{\partial r}}}_{T} + \underbrace{\frac{1}{Re}\frac{1}{r}\frac{\partial}{\partial r}\left(r\frac{\partial\overline{u'^2}}{\partial r}\right)}_{D} + \underbrace{2\overline{p'\frac{\partial u'}{\partial z}}}_{\Pi}$$
$$\underbrace{-\frac{2}{Re}\overline{\left[\left(\frac{\partial u'}{\partial r}\right)^2 + \frac{1}{r^2}\left(\frac{\partial u'}{\partial\theta}\right)^2 + \left(\frac{\partial u'}{\partial z}\right)^2\right]}}_{-\epsilon} = 0; \tag{4.6}$$

$$\overline{v'^2}\text{-budget} \quad \underbrace{-\frac{1}{r}\frac{\partial(r\overline{v'^2v'})}{\partial r} + \frac{2}{r}\overline{v'w'^2}}_{T} + \underbrace{\frac{1}{Re}\left[\frac{1}{r}\frac{\partial}{\partial r}\left(r\frac{\partial\overline{v'^2}}{\partial r}\right) + \frac{2}{r^2}(\overline{w'^2} - \overline{v'^2})\right]}_{D}$$
$$\underbrace{-2\overline{v'\frac{\partial p'}{\partial r}}}_{\Pi} \underbrace{-\frac{2}{Re}\overline{\left[\left(\frac{\partial v'}{\partial z}\right)^2 + \left(\frac{\partial v'}{\partial r}\right)^2 + \frac{1}{r^2}\left(\frac{\partial v'}{\partial\theta}\right)^2\right]}}_{-\epsilon} = 0; \tag{4.7}$$

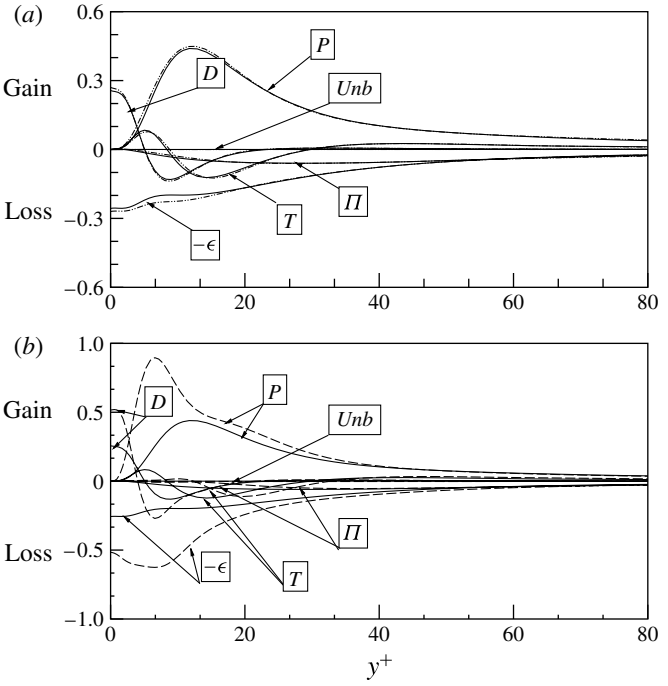

FIGURE 14. Streamwise velocity fluctuation energy budget. ——, ST case; — · —, CD case; and – – – –, WD2 case.

$$\overline{w'^2}\text{-budget} \quad \underbrace{-\frac{1}{r}\frac{\partial(r\overline{v'w'^2})}{\partial r}-\frac{2}{r}\overline{v'w'^2}}_{T}+\underbrace{\frac{1}{Re}\left[\frac{1}{r}\frac{\partial}{\partial r}\left(r\frac{\partial\overline{w'^2}}{\partial r}\right)-\frac{2}{r^2}(\overline{w'^2}-\overline{v'^2})\right]}_{D}$$
$$+\underbrace{\frac{2}{r}\overline{p'\frac{\partial w'}{\partial\theta}}}_{\Pi}\underbrace{-\frac{2}{Re}\left[\overline{\left(\frac{\partial w'}{\partial z}\right)^2}+\overline{\left(\frac{\partial w'}{\partial r}\right)^2}+\overline{\frac{1}{r^2}\left(\frac{\partial w'}{\partial\theta}\right)^2}\right]}_{-\epsilon}=0. \tag{4.8}$$

The terms P, T, D, ϵ and Π appearing in (4.6)–(4.8) are presented in inner coordinates in figures 14, 16 and 17. The distributions of the various terms in these budgets in the ST case agree well with those of Eggels *et al.* (1994) and Orlandi & Ebstein (2000).

In figure 14(*a*) the budget of $\overline{u'^2}$ shows that, for $y^+ \geqslant 30$, the production is equally balanced by dissipation and pressure transport, the latter tending to make the flow isotropic. Approaching the wall, the turbulent transport and viscous diffusion rates again become positive (producing terms) at $y^+ \approx 8$ and $y^+ \approx 5$, respectively. In that region, the dissipation rate and viscous diffusion are the leading terms, which balance each other at the wall. The current-dominated case is very similar to the steady one, except for minor differences in the P and ϵ terms for $y^+ < 15$. As discussed later, some of the above differences may be explained in terms of the effects of the unsteady modulation of the shear stress. In the $\beta = 10.6$ case (see figure 14*b*), the largest differences occur in the first 30 wall units. First production (dissipation) increases (decreases) considerably with respect to the ST case for $y^+ < 15$ ($y^+ < 30$),

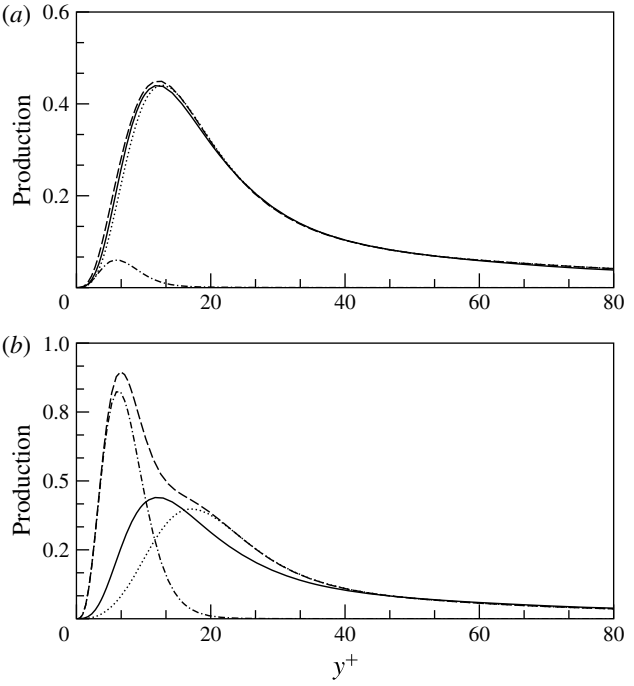

FIGURE 15. Radial distribution of production terms, for the (*a*) CD case and (*b*) WD2 case: · · · · · ·, P_c; — · —, P_o; – – – –, P; and ——, production in the steady case.

reaching a maximum (minimum) at $y^+ \sim 7$. While the peak production value is nearly doubled, its location is displaced towards the wall direction, and it is balanced by a local minimum in the dissipation. Unlike the ST case, where the $-\epsilon$ minimum occurs at the wall, in the WD2 case the presence of a minimum far from the wall is observed. The latter is closely related to the already mentioned large increase in the P term, a phenomenon peculiar to the rapid oscillation (type V) regime, and connected with the interaction between the large-amplitude unsteady forcing and the shear stress modulation. To prove the above claim, we decompose the production term as

$$P = P_c + P_o = -2\overline{u'v'}\frac{\mathrm{d}\overline{u}}{\mathrm{d}r} - 2\widetilde{\overline{u'v'}}\frac{\mathrm{d}\widetilde{u}}{\mathrm{d}r}, \tag{4.9}$$

which follows from the P definition accounting for

$$\langle\cdot\rangle = \bar{\cdot} + \tilde{\cdot} \quad \text{and} \quad \bar{\tilde{\cdot}} = 0, \tag{4.10}$$

and report in figure 15 the individual contributions and the overall production terms, for both current- and wave-dominated cases. As the data clearly show, in the WD2 case the rate of production of turbulent energy P_o by $\widetilde{u'v'}$ is present in the first 20 wall units and is dominant for $y^+ < 10$. The rate of production of turbulent energy P_c by $\overline{u'v'}$ is similar to the production term in the steady case, with a displacement of ∼5 wall units in the maximum position and a slight amplitude reduction. This agrees well with the increased extent of the quasi-streamwise vortices suggested by the streamwise vorticity distribution (see figure 11).

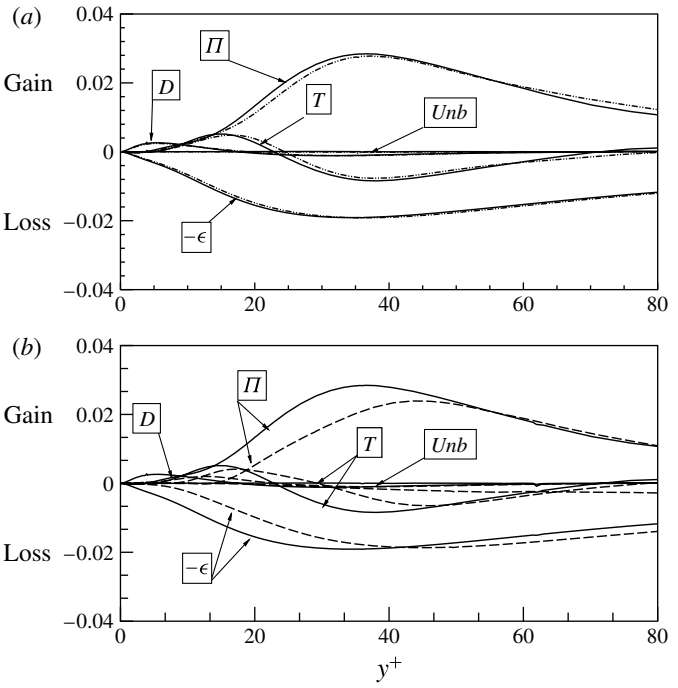

FIGURE 16. Radial velocity fluctuation energy budget. For curves, see figure 14.

Acronym	$\mathscr{P}_c^+$	$\mathscr{P}_o^+$	$\mathscr{P}^+$
ST	0.114	—	0.114
CD	0.111	0.004	0.115
WD2	0.117	0.076	0.193

TABLE 7. Volume-averaged turbulent kinetic energy productions.

For $y^+ < 10$, the P_o term exceeds the steady value by an amount nearly equal to the $-\epsilon$ term, and therefore the viscous diffusion, which has to balance the dissipation at the wall, changes accordingly. In the CD case, the contribution of the P_o term is negligible, as shown by the slight differences in the production term distribution between the CD and the ST cases. Table 7 reports the following integral quantities:

$$\mathscr{P}^+ = \mathscr{P}_c^+ + \mathscr{P}_o^+ = \frac{1}{V}\int_V P_c^+ \,\mathrm{d}V + \frac{1}{V}\int_V P_o^+ \,\mathrm{d}V, \tag{4.11}$$

representing the volume-averaged productions, with $V = \pi R^2 L_z$ the computational volume.

The total production $\mathscr{P}^+$ increases with the oscillation up to 69.4 % in the WD2 case, while $\mathscr{P}_c^+$ is nearly constant. It is worth noting that an outer coordinate representation of the quantities reported in table 7 shows that, while the increase of $\mathscr{P}_o$ is retained, $\mathscr{P}_c$ reduces by ∼16 %.

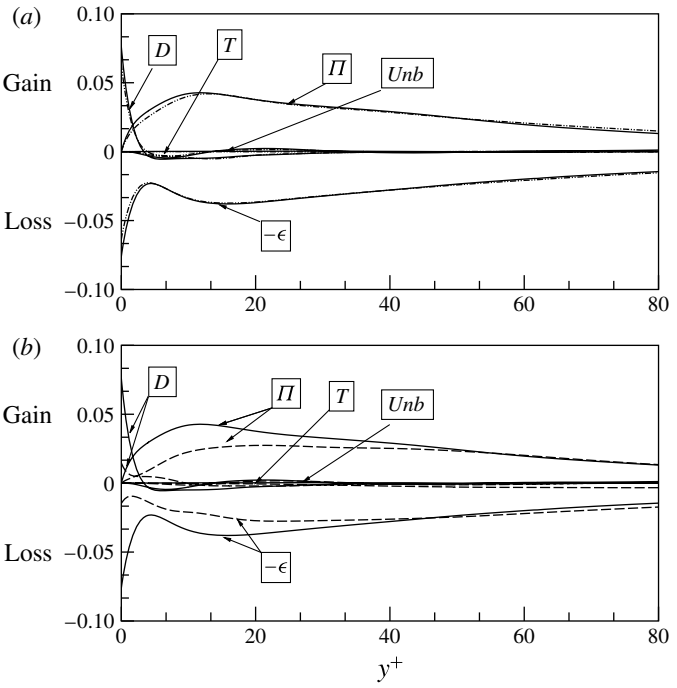

FIGURE 17. Azimuthal velocity fluctuation energy budget. For curves, see figure 14.

The velocity pressure gradient Π is one order of magnitude smaller than the leading term (P) and will be discussed later.

The budget of $\overline{v'^2}$, shown in figure 16, suggests that the velocity pressure gradient term is dominant and it mainly balances the dissipation rate for $y^+ \geqslant 70$, in both ST and CD cases. In the wall region, the turbulent transport T is producing (consuming) for $5 \leqslant y^+ \leqslant 25$ (for $25 \leqslant y^+ \leqslant 70$). For $y^+ < 5$ and $y^+ > 70$, T is again a production term. In the WD2 case, Π, T and $-\epsilon$ are seen to decrease slightly in magnitude; their peak values are displaced towards the core region by 10 wall units. Figure 17 reports the budget of $\overline{w'^2}$. For $y^+ \geqslant 4$, the dissipation rate is balanced by the velocity pressure gradient, which is the leading production term, in both CD and ST cases. Approaching the wall, Π decays and D becomes increasingly important and attains its maximum at the wall. The turbulent transport term is small compared to the other terms. In the WD2 case, similarly to the $\overline{v'^2}$ budget, a reduction of the peak and a displacement towards the pipe axis are observed.

We now return to the analysis of the velocity pressure gradient, which can be decomposed into the pressure strain Φ and pressure diffusion Ψ terms:

$$\overline{u'^2}\text{-budget} \quad \Pi = \Phi_{zz} + \Psi_{zz} = 2\overline{p'\frac{\partial u'_z}{\partial z}} + 0, \tag{4.12}$$

$$\overline{v'^2}\text{-budget} \quad \Pi = \Phi_{rr} + \Psi_{rr} = 2\overline{p'\frac{\partial u'_r}{\partial r}} - 2\overline{\frac{\partial\left(p'u'_r\right)}{\partial r}}, \tag{4.13}$$

$$\overline{w'^2}\text{-budget} \quad \Pi = \Phi_{\theta\theta} + \Psi_{\theta\theta} = \frac{2}{r}\overline{p'\left(\frac{\partial u'_\theta}{\partial \theta} + u'_r\right)} - 2\frac{\overline{p'u'_r}}{r}. \tag{4.14}$$

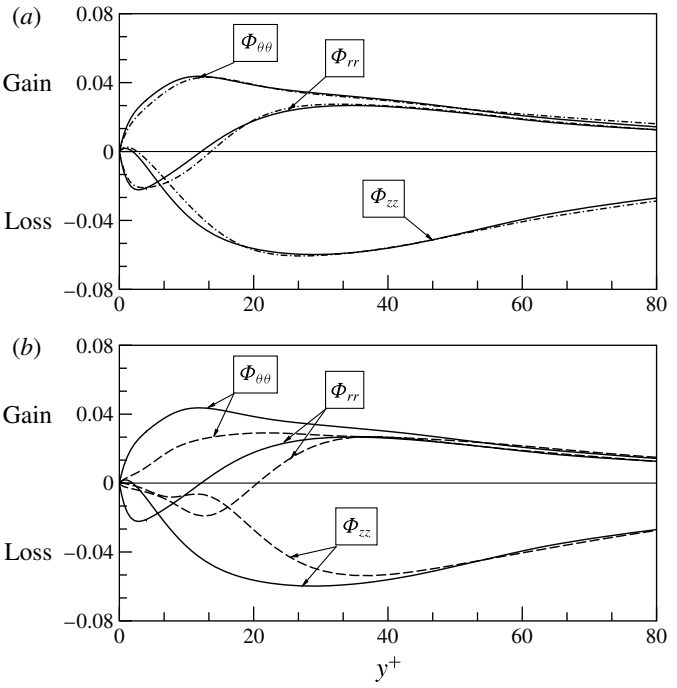

FIGURE 18. Radial distribution of pressure strain terms. For curves, see figure 14.

The pressure strain terms Φ_{zz}, Φ_{rr} and $\Phi_{\theta\theta}$, which govern the energy exchange among the three components of the turbulent kinetic energy, are shown in figure 18, in inner coordinates. Following the notation of Hinze (1975), a negative (positive) sign of, say, Φ_{zz} denotes a loss or transfer (gain) of energy from the streamwise component to the other components. While the production due to the shear only exists in the streamwise component, the two other components gain energy through this redistribution process. The current-dominated case (see figure 18*a*) does not differ from the steady one, showing a net transfer of energy from the streamwise component of turbulent velocity fluctuation to the cross-stream components, except very close to the wall. On the other hand, in the first 12 wall units, there is large energy transfer from the radial component to the streamwise and azimuthal ones; an analogous effect is referred to as 'splatting' by Moin & Kim (1981). The splatting effect is connected to sweep events carrying high-speed fluid to the wall and thus produces flow patterns similar to those of a jet impinging on the wall. Increasing β from 1 to 10.6 results in the appreciable changes reported in figure 18(*b*), for $y^+ < 50$. The reduction of Φ_{zz} entails a reduced energy transfer from the $\overline{u_z'^2}$ component to the radial and azimuthal ones. Very close to the wall, this phenomenon is magnified and leads to an anisotropy enhancement, as documented through the distribution of the second invariant of vorticity and Reynolds stress (see figure 25 of the Appendix). The pressure strain term Φ_{rr} also undergoes appreciable changes, for $y^+ < 30$. Most evident is the displacement towards the pipe core of both the negative peak and the zero-point value, which agrees well with the altered splatting mechanism observed while discussing the Q2 events in the quadrant analysis and the wall value of ω_z'.

Figures 19 and 20 report four instantaneous realizations of the velocity vector fields made dimensionless with the bulk velocity in a cross-plane with a phase interval

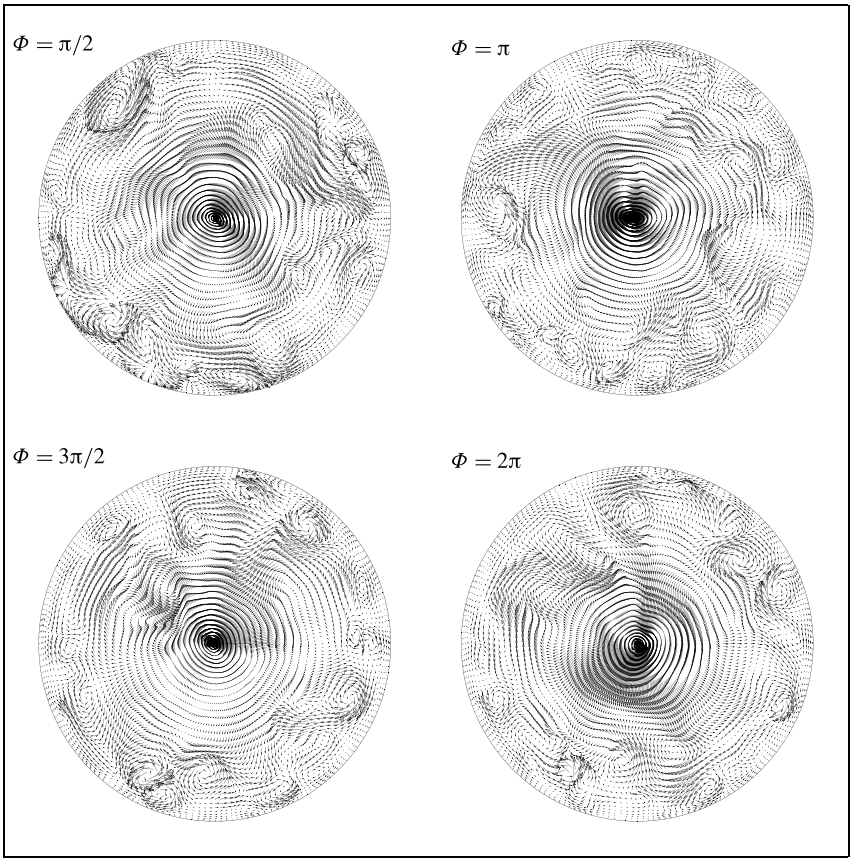

FIGURE 19. Instantaneous velocity vector fields in a cross-plane in outer coordinates (CD case).

of 90°, for the CD and WD2 cases, respectively. For the sake of ease of representation, the vector field has been interpolated on a single-domain coarser mesh. Disregarding the phase variation of the velocity vector field and concentrating on the differences between the corresponding images of figures 19 and 20, it can be easily inferred that both the number and strength of the vortical structures are considerably reduced when β is increased. Furthermore, the size of the quasi-streamwise vortices appears to be larger in the $\beta = 10.6$ case, a fact that has already been documented in the statistical sense. Figures 21 and 22 represent the counterparts of figures 19 and 20 reporting the streamwise fluctuations, made dimensionless with the bulk velocity. Again, there is a clear indication that the number of quasi-streamwise vortices is reduced while their size appears to increase with β.

Taken collectively, figures 19–22 support the idea that the magnitude of the oscillation has a definite impact on the size and strength of the streaks, a fact that will be clarified in the forthcoming paper, where the focus will be upon the analysis of their changes in phase space.

5. Conclusions

Direct numerical simulations of pulsating pipe flow in the high-frequency regime have been analysed. Both current- and wave-dominated flow conditions with a

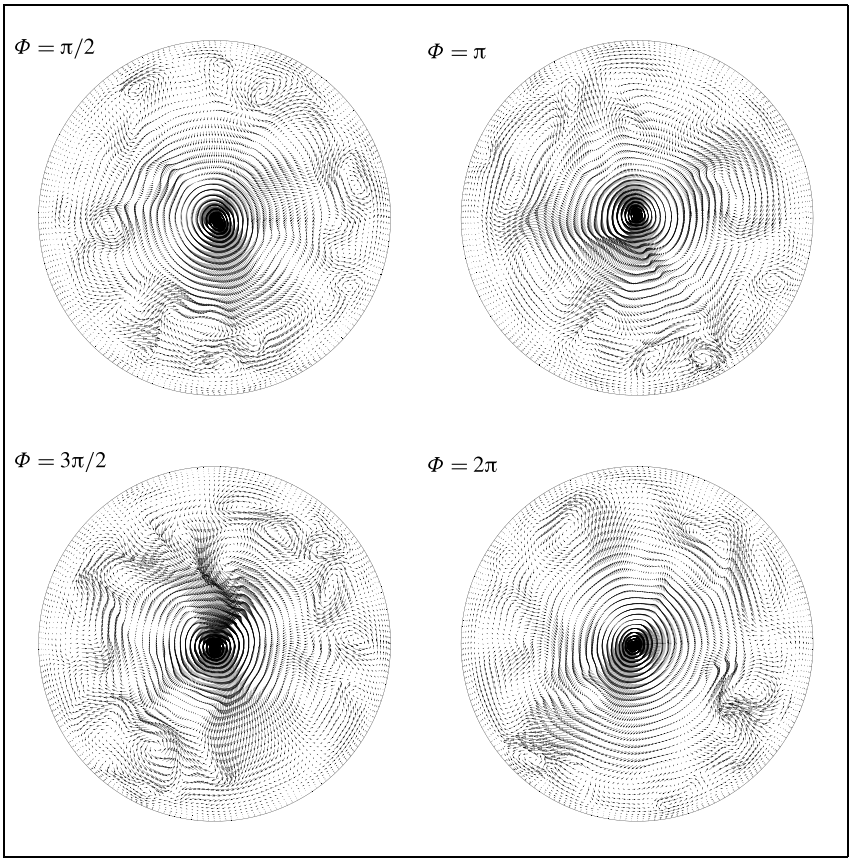

FIGURE 20. Instantaneous velocity vector fields in a cross-plane in outer coordinates (WD2 case).

fixed Stokes number have been considered. The dimensionless parameters have been selected to cover a region of the state space where a previous experimental study has documented interesting features. The data have been collected from fully resolved DNSs carried out with a spectral Chebyshev algorithm for the inhomogeneous (radial) direction and blended Fourier decomposition for the homogeneous (axial and azimuthal) ones. Four flow conditions characterized by different values of the oscillating and bulk velocity amplitude ratio β have been considered. When β is increased from 1 to 5, a turbulent to laminar reverse transition process occurs. This phenomenon, which has already been experimentally observed through a global parameter study by Lodahl *et al.* (1998), has been confirmed by the present work. A further increase of β up to 10.6 leads again to turbulent conditions of the mean flow accompanied by a remarkable reduction of the cycle-averaged friction coefficient compared to the steady value. The mean velocity profile shows a logarithmic region with a slope essentially equal to the corresponding steady one, but characterized by an upward shift, a consequence of an increase in thickness of the viscous sublayer. Conversely, it has been shown that the oscillating flow obeys the Stokes solution and therefore the flow appears to be one way coupled. The radial distributions of the mean normal stress components shed light on a different split of the individual

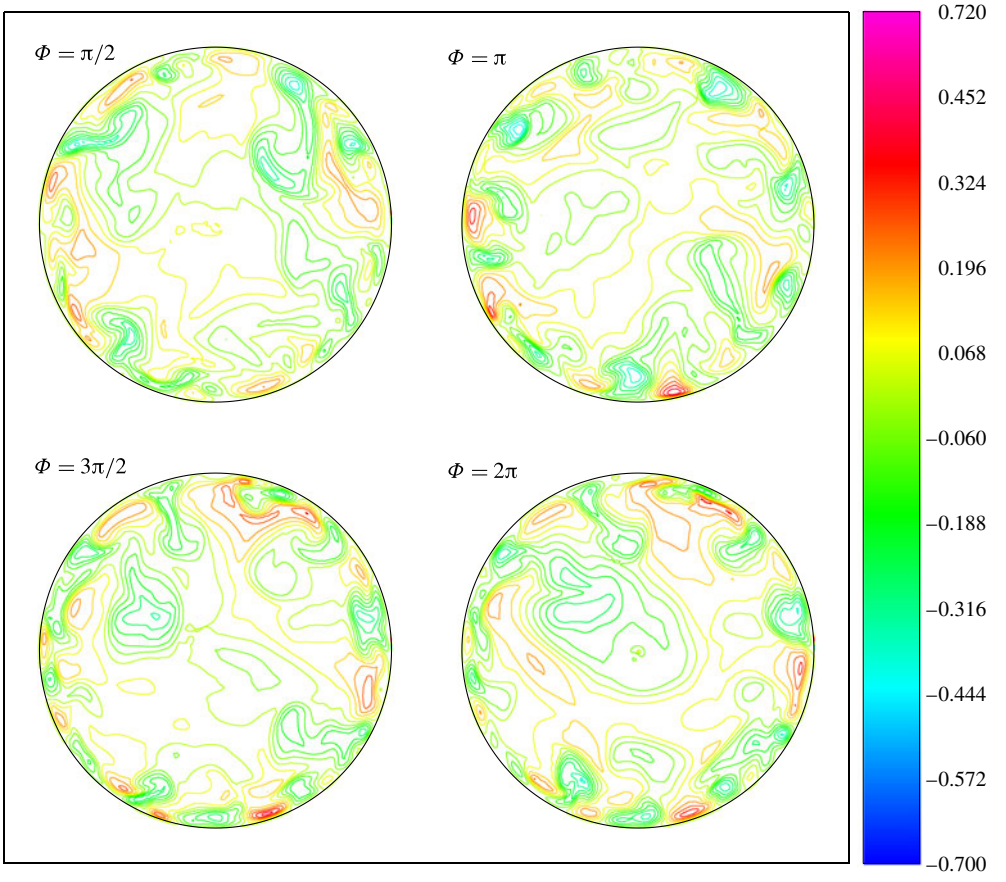

FIGURE 21. Instantaneous contours of streamwise velocity fluctuations in outer coordinates in a cross-plane (CD case).

contributions compared to the non-pulsating case at the same bulk Reynolds number. Likewise, in the wall layer, a considerable reduction of the structure parameter is observed. The radial distribution of the streamwise vorticity fluctuation suggests a nearly double radial extent of the streamwise vortices, a fact that entails a reduction in the turbulence production mechanism as dictated by the near-wall streaks dynamics. The latter has been altered through a reduced contribution of sweeps in the first 20 wall units. The streamwise velocity fluctuation budget showed a remarkable change of the production and dissipation terms in the buffer layer and below, an effect of the interaction between the large-amplitude unsteady forcing and the shear stress modulation. The analysis of the diagonal components of the pressure strain tensor controlling the energy exchange among the three components of the turbulent kinetic energy suggested an alteration in the transfer of energy from the streamwise to the radial and azimuthal components. Likewise, close to the wall, appreciable changes in the splatting mechanism are observed. The above results taken collectively indicate an enhanced turbulence anisotropy in a region of the wall layer extending at least up to 30 wall units.

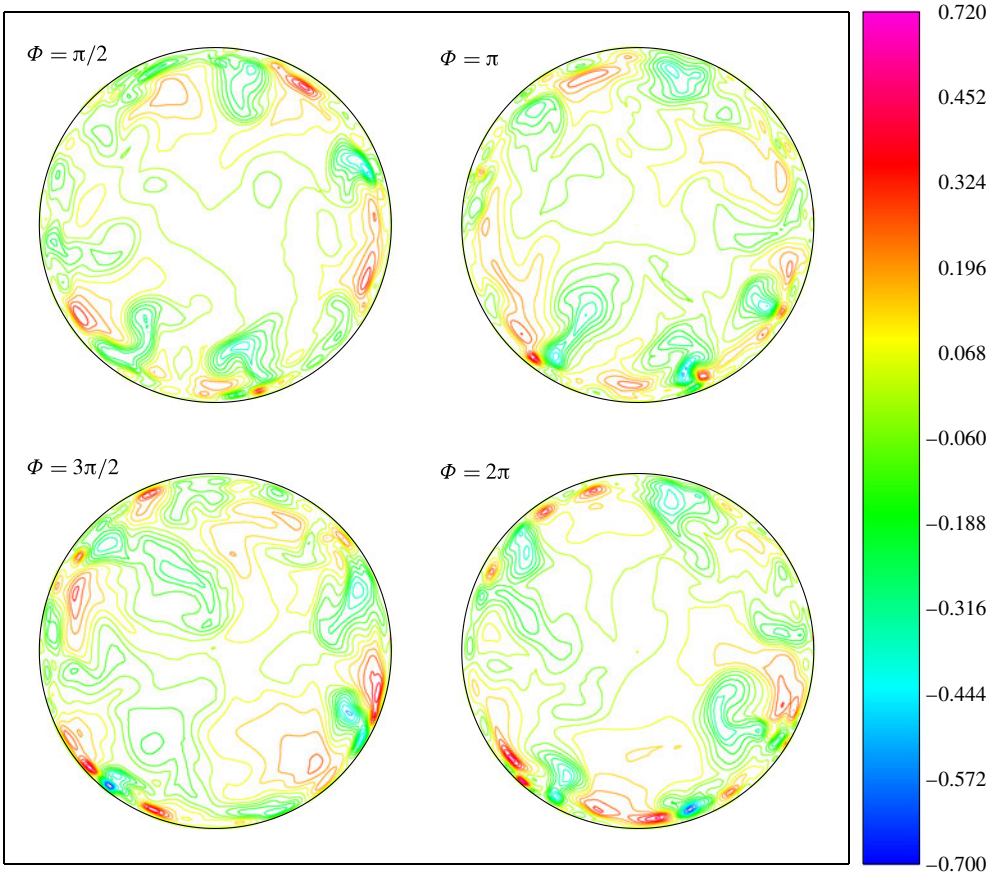

FIGURE 22. Instantaneous contours of streamwise velocity fluctuations in outer coordinates in a cross-plane (WD2 case).

This paper has been completely devoted to the analysis of the time- and space-averaged features, since within this context the authors have already found many interesting physical phenomena whose comparison with the statistically steady turbulent pipe flow has turned out to be instructive. In addition, the wealth of data presented and analysed can be considered as a benchmark for those researchers aiming at validating new numerical procedures or novel measurement techniques against accurate and reliable data.

Although this study was focused only on the time- and space-averaged statistics, the authors are aware that, owing to the periodic nature of the flow, a phase-averaged analysis is also necessary in order to fully unravel the flow dynamics. This additional investigation is being carried out and will be the topic of a forthcoming paper.

Acknowledgements

The authors are indebted to Professors P. Blondeaux, U. Piomelli and M. Quadrio for their comments and remarks on a preliminary draft of the paper and for their valuable advice during the preparation of the final manuscript. Some of the simulations

presented in this paper have been run at the computing centre CASPUR in Rome; the authors gratefully acknowledge the support of the centre.

Appendix. Invariant analysis

In this appendix we further elaborate on the large anisotropy of the wall layer, by examining the Reynolds stress and vorticity anisotropy tensors, respectively defined as

$$b_{ij} = \frac{\overline{u_i' u_j'}}{2\kappa} - \frac{\delta_{ij}}{3}, \quad v_{ij} = \frac{\overline{\omega_i' \omega_j'}}{\overline{\omega'^2}} - \frac{\delta_{ij}}{3}, \tag{A 1}$$

where $\overline{\omega'^2} = \overline{\omega_i' \omega_i'}$ is the mean square vorticity or the mean square enstrophy. In figures 23 and 24 the computed second and third invariants of the two tensors

$$II_b = -\tfrac{1}{2} b_{ij} b_{ji}, \quad II_v = -\tfrac{1}{2} v_{ij} v_{ji}, \tag{A 2}$$

$$III_b = \tfrac{1}{3} b_{ij} b_{jk} b_{ki}, \quad III_v = \tfrac{1}{3} v_{ij} v_{jk} v_{ki} \tag{A 3}$$

are shown, for all simulations, in the Lumley triangle defined by the limiting values of (A 2) and (A 3) and constituting the anisotropy invariant map (AIM) (Lumley & Newman 1977). These limiting values satisfy the following conditions:

$$\begin{aligned} &\text{isotropic turbulence} && III = 0, \quad -II = 0, \\ &\text{axisymmetric turbulence} && A \equiv \frac{\frac{1}{2} III}{(-\frac{1}{3} II)^{3/2}} = \pm 1, \\ &\text{two-component turbulence} && G \equiv 27III + 9II + 1 = 0, \\ &\text{one-component turbulence} && III = \tfrac{2}{27}, \quad -II = \tfrac{1}{3}. \end{aligned} \tag{A 4}$$

While the two-component state appears as a straight line in the AIM, there are two branches defining the axisymmetric turbulence, namely disc-like (the turbulence is pulled out in two directions and is squeezed in the other direction; $A_b = 1$ and $A_v = -1$) and rod-like (the turbulence may be represented by elongated vortical structures; $A_b = -1$ and $A_v = 1$) (Lee & Reynolds 1985). Even though the AIMs carry information only about the turbulence components (*componentiality*) and therefore do not contain information about the *dimensionality* of the turbulence, they are useful tools to better characterize the energy-producing events in the near-wall region where anisotropy is maximum (Reynolds & Kassinos 1995). In the Lumley plane, the degree of anisotropy is associated with changes in the $-II$ invariant, a non-negative quantity, whereas the nature of the anisotropy is indicated by variations of the III invariant (Oyewola, Djenidi & Antonia 2004).

As already noted from the analysis of other statistical quantities, the ST and CD cases do not differ much from each other. In the near-wall region, the turbulence has, as expected, two dominant components and the computed data closely follow the $G = 0$ line. Starting from the wall, the anisotropy invariants of both tensors point towards the right top cusp describing one-component turbulence. As shown in table 8, the wall distance where the $(III, -II)$ pair reaches a maximum for the Reynolds stress (vorticity) anisotropy tensor is found to be $y^+ \sim 8$ and $y^+ \sim 7$ in the ST and CD cases ($y^+ \sim 3$ and $y^+ \sim 2$). Afterwards, for both tensors, the III and $-II$ invariants start to decrease and approach the right boundary, actually reaching it for the vorticity at $y^+ \sim 4$. Moving further away from the wall, the $(III_b, -II_b)$ pair tends monotonically to the origin, i.e. to the isotropic state. Conversely, the $(III_v, -II_v)$ pair first reaches the bottom left boundary at $y^+ \sim 24$ and then arrives at the near bottom cusp region.

	Wall values			Point of maximum anisotropy			
	y^+_{wall}	$(III, -II)_b$	$(III, -II)_v$	y^+_b	$(III, -II)_b$	y^+_v	$(III, -II)_v$
$\beta = 0$	0.08	(0.02, 0.16)	(0.02, 0.16)	8.2	(0.04, 0.24)	2.8	(0.04, 0.22)
$\beta = 1$	0.08	(0.02, 0.18)	(0.02, 0.18)	7.3	(0.05, 0.25)	2.3	(0.04, 0.23)
$\beta = 10.6$	0.06	(0.07, 0.31)	(0.07, 0.31)	3.6	(0.07, 0.32)	0.55	(0.07, 0.31)

TABLE 8. Wall (left) and maximum anisotropy (right) values.

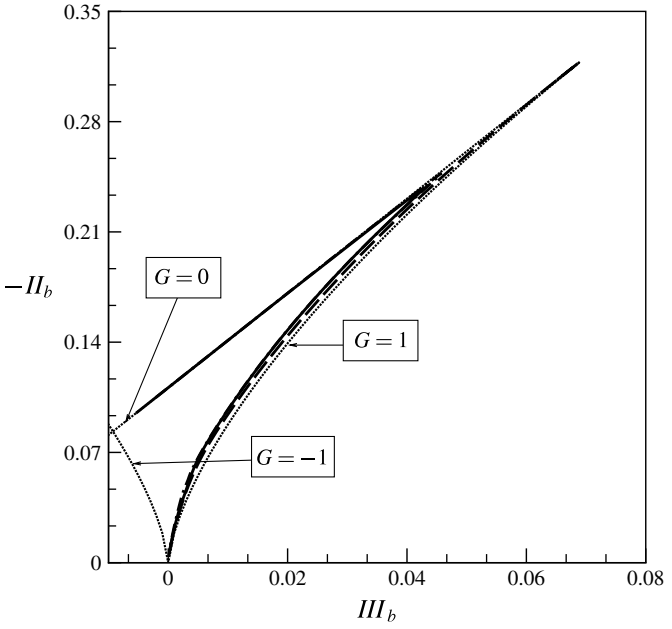

FIGURE 23. Anisotropy-invariant map of the Reynolds stress tensor. For curves, see figure 9.

The WD2 data considerably differ from those for ST and CD in three main respects. First, in the near-wall region, the amplitude of the oscillation increases the anisotropy, as evident from the closeness of the first grid point to the upper right cusp in the WD2 case (see figures 23 and 24 and table 8). Second, for both tensors, the $-II$ maximum values occur at a distance closer to the wall and are much closer to the one-component limit (0.07, 0.33) as shown in table 8.

Finally, in the buffer region and above, there is an appreciable tendency to a more anisotropic behaviour documented by the increased $-II$ values, independently of the wall distance, as β increases up to 10.6. The above argument is shown on a quantitative basis by the $-II$ distributions in the wall-normal direction presented in figure 25, in inner coordinates. The data have been normalized with the one-component turbulence value $AI = II/II_{1D}$, so that the closeness to unity of AI is a measure of the one-dimensionality of the turbulence; likewise, an isotropic state corresponds to $AI = 0$. Information buried in figure 25, taken collectively, supports the fact that the main effect of the amplitude of the oscillation for a fixed frequency consists of an enhanced turbulence anisotropy in a region of the wall layer extending

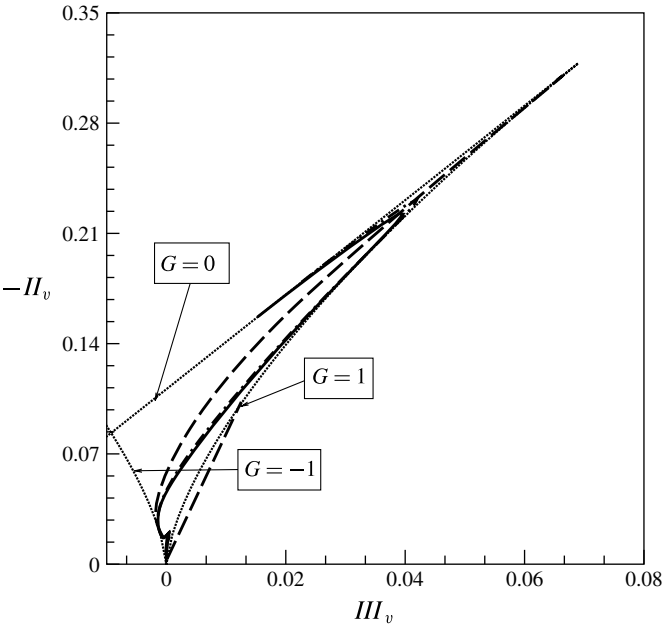

FIGURE 24. Anisotropy-invariant map of the vorticity tensor. For curves, see figure 8.

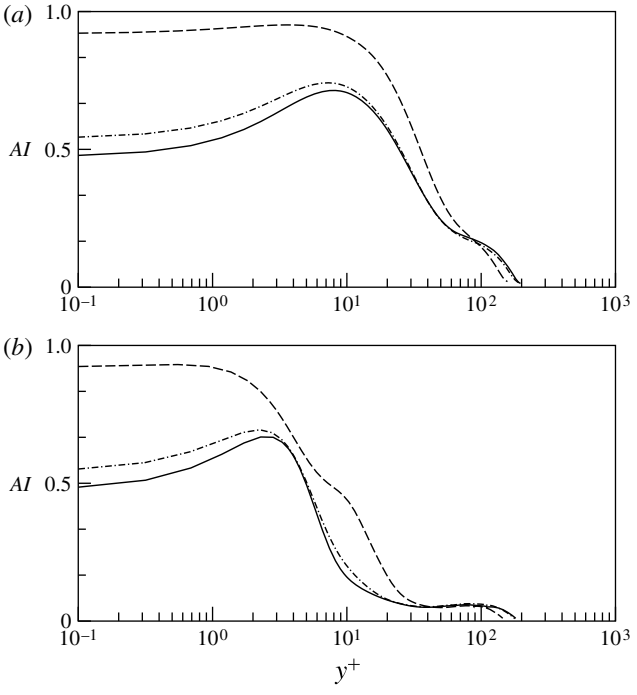

FIGURE 25. Radial distributions of the anisotropy index *AI*: (*a*) Reynolds stress tensor; and (*b*) vorticity tensor. For curves, see figure 9.

at least up to 30 wall units for both tensors and therefore far beyond the Stokes layer thickness $\delta^+ = 3$. These changes alter the contribution to the total turbulence production described by the various events connected to the Reynolds shear stress, as already discussed § 4. This remarkable anisotropy increase is common to many drag reducing flows, such as turbulent channel and boundary layer flows, as reported by Frohnapfel *et al.* (2007), who showed through the analysis of a few datasets of experimental and numerical nature that the turbulence anisotropy increases and tends to the one-component limit in the near-wall region. The same trend is observed when the Reynolds number is reduced.

REFERENCES

ABRAMOWITZ, M. & STEGUN, I. A. 1972 *Handbook of Mathematical Functions*. Dover.

AKHAVAN, R., KAMM, R. D. & SHAPIRO, A. H. 1991 An investigation of transition to turbulence in bounded oscillatory Stokes flows. Part 1. Experiments. *J. Fluid Mech.* **225**, 395–442.

BARENBLATT, G. I. 1993*a* Scaling laws for fully developed shear flows. Part 1. Basic hypotheses and analysis. *J. Fluid Mech.* **248**, 513–520.

BARENBLATT, G. I. 1993*b* Scaling laws for fully developed shear flows. Part 2. Processing of experimental data. *J. Fluid Mech.* **248**, 521–529.

BHAGANAGAR, K. 2008 Direct numerical simulation of unsteady flow in channel with rough walls. *Phys. Fluids* **20**, 101508.

BINDER, G. & KUENY, J. L. 1981 Measurements of the periodic velocity oscillations near the wall in unsteady turbulent channel flow. In *Unsteady Turbulent Shear Flow* (ed. R. Michel, J. Cousteix & R Houdeville), pp. 100–109. Springer.

BINDER, G., TARDU, S. F. & VEZIN, P. 1995 Cyclic modulation of Reynolds stresses and length scales in pulsed turbulent channel flow. *Proc. R. Soc. Lond.* A **451** (1941), 121–139.

BLACKWELDER, R. F. & HARITONIDIS, J. H. 1983 Scaling of the bursting frequency in turbulent boundary layers. *J. Fluid Mech.* **132**, 87–103.

BLEL, W., LE GENTIL-LELIEVREB, C., BÉNÉZECHB, T. & LEGENTILHOMME, P. 2009 Application of turbulent pulsating flows to the bacterial removal during a cleaning in place procedure. Part 1. Experimental analysis of wall shear stress in a cylindrical pipe. *J. Food Engng* **90** (4), 422–432.

BRERETON, G. J., REYNOLDS, W. C. & JAYARAMAN, R. 1990 Response of a turbulent boundary layer to sinusoidal free stream unsteadiness. *J. Fluid Mech.* **221**, 131–159.

CHOI, K. S. 1989 Near-wall structure of a turbulent boundary layer with riblets. *J. Fluid Mech.* **208**, 417–459.

EGGELS, J. G. M., UNGER, F., WEISS, M. H., WESTERWEEL, J., ADRIAN, R. J., FRIEDRICH, R. & NIEUWSTADT, F. T. M. 1994 Fully developed turbulent pipe flow: a comparison between direct numerical simulation and experiment. *J. Fluid Mech.* **268**, 175–210.

FEDELE, F., HITT, D. L. & PRABHUB, R. D. 2005 Revisiting the stability of pulsatile pipe flow. *Eur. J. Mech.* (B/*Fluids*) **24**, 237–254.

FROHNAPFEL, B., LAMMERS, P., JOVANOVIĆ, J. & DURST, F. 2007 Interpretation of the mechanism associated with turbulent drag reduction in terms of anisotropy invariants. *J. Fluid Mech.* **577**, 457–466.

GILBRECH, D. A. & COOMBS, G. D. 1963 Critical Reynolds numbers for incompressible pulsating flow in tubes. *Dev. Theor. Appl. Mech.* **1**, 292–304.

GROSCH, C. E. & SALWEN, H. 1968 The stability of steady and time-dependent plane Poiseuille flow. *J. Fluid Mech.* **34** (1), 177–205.

HALL, P. 1975 The stability of Poiseuille flow modulated at high frequencies. *Proc. R. Soc. Lond.* A **344** (1639), 453–464.

HE, S. & JACKSON, J. D. 2009 An experimental study of pulsating turbulent flow in a pipe. *Eur. J. Mech.* (B/*Fluids*) **28**, 309–320.

HERBERT, D. M. 1972 The energy balance in modulated plane Poiseuille flow. *J. Fluid Mech.* **56** (1), 73–80.

HINZE, J. O. 1975 *Turbulence*. McGraw-Hill.

HWANG, J.-L. & BRERETON, G. J. 1991 Turbulence in high-frequency periodic fully-developed pipe flow. In *Eighth International Symposium on Turbulent Shear Flows* (ed. F. Durst, R. Friedrich, B. E. Launder, F. W. Schmidt, U. Schuman & J. H. Whitelaw). Springer.

VON KERCZEK, C. H. 1982 The instability of oscillatory plane Poiseuille flow. *J. Fluid Mech.* **116**, 91–114.

KIM, J., MOIN, P. & MOSER, R. 1987 Turbulence statistics in fully developed channel flow at low Reynolds number. *J. Fluid Mech.* **177**, 133–166.

LEE, M. & REYNOLDS, W. 1985 Numerical experiments on the structure of homogeneous turbulence. *Tech. Rep.* TF-24. Thermoscience Division, Stanford University.

LODAHL, C. R., SUMER, B. M. & FREDOSOE, J. 1998 Turbulent combined oscillatory flow and current in a pipe. *J. Fluid Mech.* **373**, 313–348.

LUCHIK, T. S. & TIEDERMAN, W. G. 1987 Timescale and structure of ejections and burst in turbulent channel flow. *J. Fluid Mech.* **174**, 529–552.

LUMLEY, J. L. & NEWMAN, G. 1977 The return to isotropy of homogeneous turbulence. *J. Fluid Mech.* **82**, 161–178.

MANNA, M. & VACCA, A. 1999 An efficient method for the solution of the incompressible Navier–Stokes equations in cylindrical geometries. *J. Comput. Phys.* **151**, 563–584.

MANNA, M. & VACCA, A. 2005 Resistance reduction in pulsating turbulent pipe flow. *Trans. ASME: J. Engng Gas Turbines Power* **127**, 410–417.

MANNA, M. & VACCA, A. 2007 Spectral dynamic of pulsating turbulent pipe flow. *Comput. Fluids* **37**, 825–835.

MANNA, M. & VACCA, A. 2009 Torque reduction in Taylor–Couette flows subject to an axial pressure gradient. *J. Fluid Mech.* **639**, 373–401.

MAO, Z. X. & HANRATTY, T. J. 1986 Studies of the wall shear stress in a turbulent pulsating pipe flow. *J. Fluid Mech.* **170**, 545–564.

MAO, Z. X. & HANRATTY, T. J. 1994 Influence of large-amplitude oscillations on turbulent drag. *AIChE J.* **40** (10), 1601–1610.

MIZUCHINA, T., MARUYAMA, T & SHIOZAKI, Y. 1973 Pulsating turbulent flow in a tube. *J. Chem. Engng Japan* **6**, 487–495.

MIZUSHINA, T., MARUYAMA, T. & HIRASAWA, H. 1975 Structure of the turbulence in pulsating pipe flows. *J. Chem. Engng Japan* **8**, 210–216.

MOIN, P. & KIM, J. 1981 Numerical investigation of turbulent channel flow. *J. Fluid Mech.* **118**, 341–377.

MOSER, R., KIM, J. & MANSOUR, N. N. 1999 Direct numerical simulation of turbulent channel flow up to $Re_\tau = 590$. *Phys. Fluids* **177**, 133–166.

MOSER, R. D. & MOIN, P. 1984 Direct numerical simulation of curved channel flow. TM 85974. NASA.

ORLANDI, P. & EBSTEIN, D. 2000 Turbulent budgets in rotating pipes by DNS. *Intl J. Heat Fluid Flow* **21**, 499–505.

ORLANDI, P. & FATICA, M. 1997 Direct simulations of a turbulent pipe rotating along the axis. *J. Fluid Mech.* **343**, 43–72.

OYEWOLA, O., DJENIDI, L. & ANTONIA, R. A. 2004 Influence of localised wall suction on the anisotropy of the Reynolds stress tensor in a turbulent boundary layer. *Exp. Fluids* **37**, 187–193.

PTASINSKI, P. K., BOERSMA, B. J., NIEUWSTADT, F. T. M., HULSEN, M. A., VAN DEN BRULE, B. H. A. A. & HUNT, J. C. R. 2003 Turbulent channel flow near maximum drag reduction: simulations, experiments and mechanisms. *J. Fluid Mech.* **490**, 251–291.

QUADRIO, M., RICCO, P. & VIOTTI, C. 2009 Streamwise travelling waves of spanwise wall velocity for turbulent drag reduction. *J. Fluid Mech.* **627**, 161–178.

QUADRIO, M. & SIBILLA, S. 2000 Numerical simulation of turbulent flow in a pipe oscillating around its axis. *J. Fluid Mech.* **424**, 217–241.

RAMAPRIAN, B. R. & TU, S. W. 1980 An experimental study of oscillatory pipe flow at transitional Reynolds number. *J. Fluid Mech.* **100**, 513–544.

RAMAPRIAN, B. R. & TU, S. W. 1983 Fully developed periodic turbulent pipe flow. Part 2. The detailed structure of the flow. *J. Fluid Mech.* **137**, 59–81.

REYNOLDS, W. C. & KASSINOS, S. C. 1995 One-point modelling of rapidly deformed homogeneous turbulence. *Proc. R. Soc. Lond.* A **451**, 87–104.

RONNEBERGER, D. & AHRENS, C. D. 1977 Wall shear stress caused by signal amplitude perturbations of turbulent boundary-layer flow: an experimental investigation. *J. Fluid Mech.* **83**, 433–464.

SARPKAJA, T. 1966 Experimental determination of the critical Reynolds number for pulsating Poiseuille flow. *Trans. ASME: J. Basic Engng* **88**, 589–598.

SCOTTI, A. & PIOMELLI, U. 2001 Numerical simulation of pulsating turbulent channel flow. *Phys. Fluids* **13** (5), 1367–1384.

SHEMER, L. 1985 Laminar–turbulent transition in a slowly pulsating pipe flow. *Phys. Fluids* **28**, 3506–3509.

SHEMER, L. & KIT, E. 1984 An experimental investigation of the quasisteady turbulent pulsating flow in a pipe. *Phys. Fluids* **27**, 72–76.

SHEMER, L., WYGNANSKI, I. & KIT, E. 1985 Pulsating flow in a pipe. *J. Fluid Mech.* **153**, 313–337.

SINGER, B., FERZIGER, J. H. & REED, H. 1989 Numerical simulation of transition in oscillatory plane channel flow. *J. Fluid Mech.* **208**, 44–66.

STETTLER, J. C. & HUSSAIN, A. K. M. F. 1986 On transition of the pulsatile flow. *J. Fluid Mech.* **170**, 169–197.

TARDU, S. F. & BINDER, G. 1993 Wall shear stress modulation in unsteady turbulent channel flow with high imposed frequencies. *Phys. Fluids* **5**, 2028–2034.

TARDU, S. F., BINDER, G. & BLACKWELDER, R. F. 1994 Turbulent channel flow with large-amplitude velocity oscillations. *J. Fluid Mech.* **267**, 109–151.

TOZZI, J. T. & VON KERCZEK, C. H. 1986 The stability of oscillatory Hagen–Poiseuille flow. *Trans. ASME: J. Appl. Mech.* **53**, 187–192.

TU, S. W. & RAMAPRIAN, B. R. 1983 Fully developed periodic turbulent pipe flow. Part 1. Main experimental results and comparison with predictions. *J. Fluid Mech.* **137**, 31–58.

TUZI, R. & BLONDEAUX, P. 2008 Intermittent turbulence in a pulsating pipe flow. *J. Fluid Mech.* **599**, 51–79.

VAN KAN, J. 1986 A second-order accurate pressure correction scheme for viscous incompressible flow. *J. Sci. Stat. Comput.* **7**, 870–891.

VIOTTI, C., QUADRIO, M. & LUCHINI, P. 2009 Streamwise oscillation of spanwise velocity at the wall for turbulent drag reduction. *Phys. Fluid* **21**, 115109.

WALLACE, J. M., ECKLMANN, H. & BRODKEY, R. S. 1972 The wall region in turbulent shear flow. *J. Fluid Mech.* **54**, 39–48.

WILLMARTH, W. W. & LU, S. S. 1972 Structure of the Reynolds stress near the wall. *J. Fluid Mech.* **55**, 65–92.

YELLIN, E. L. 1966 Laminar–turbulent transition process in pulsatile flow. *Circulat. Res.* **19**, 791–804.

ZAGAROLA, M. V. & SMITS, A. J. 1998 Mean flow scaling of turbulent pipe flow. *J. Fluid Mech.* **373**, 33–79.

ZOU, L. Y., LIU, N. S. & LU, X. Y. 2006 An investigation of pulsating turbulent open channel flow by large eddy simulation. *Comput. Fluids* **35** (1), 74–102.